Structure and Lattice Dynamics of Copper- and Silver-based Superionic Conducting Chalcogenides

Vom Fachbereich Material- und Geowissenschaften
der Technischen Universität Darmstadt

zur Erlangung des akademischen Grades
Doktor der Naturwissenschaften (Dr. rer. nat.)
genehmigte Dissertation

vorgelegt von

Dipl.-Ing. Dmytro M. Trots
aus Kowel, Ukraine

Berichterstatter: Prof. Dr.-Ing. Dr. h.c. H. Fueß
Mitberichterstatter: Prof. Dr. W. Ensinger
Tag der Einreichung: 11.04.2007
Tag der mündlichen Prüfung: 25.05.2007

Darmstadt 2007
D 17

Dedicated to my grandfathers S. Rudnytskii and V. G. Trots

Contents

Chapter 1

Thesis outline

Superionic conductors are compounds that exhibit exceptionally high values of ionic conductivity within the solid state [1,2]. There are no rigid definitions of whether a given material is superionic or not. It is, however, generally accepted that the superionics are materials whose ionic conductivity is above $\sigma \sim 10^{-2}\ \Omega^{-1}\cdot\mathrm{cm}^{-1}$, with the best superionic conductors achieving conductivities of $\sigma \sim 1\ \Omega^{-1}\cdot\mathrm{cm}^{-1}$ or better [2]. A correlation of microscopic structural properties with macroscopic ionic conductivity which achieves liquid-like values and a possible mechanisms of ionic transport through the structure are crucial points in investigations of crystalline superionics. A number of methods to determine structural properties and disorder in superionic conductors were therefore developed. They are entirely described in a modern review by D.A. Keen [2], moreover, a current state of science concerning crystal structures and conduction processes in superionic conductors was well considered in a more recent review by S. Hull [1]. Superionic conductors are not merely of scientific interest, since compounds with high ionic conductivities have a number of technological applications. There are a number of papers on applications of superionics within solid state batteries [3,4], high power fuel cells [5,6] and fast-response gas sensors [7,8]. All foregoing topics will be therefore not reviewed in this thesis.

The present thesis is dedicated to high-temperature investigations of superionic copper- and/or silver- based selenides, $Cu_{2-\delta}Se$ with $\delta = 0$, 0.15, 0.25 and AgCuSe, as well as on copper- and silver- based sulfides, AgCuS and Ag_3CuS_2. These studies were consistent with the following strategy: synthesis $\longrightarrow$ preliminary characterization of the samples $\longrightarrow$ high-

temperature synchrotron and/or neutron diffraction $\longrightarrow$ inelastic neutron scattering. A short literature survey of results on temperature dependencies of ionic conductivity and on structural investigations are presented in chapter 2 of this work together with their motivation. The experimental details of the syntheses of the samples, simultaneous thermal analysis (STA), conventional X-ray, synchrotron and neutron diffraction as well as inelastic neutron scattering (INS) measurements are described in chapter 3. The details of data treatment are also given in this chapter. In order to check phase purity of the samples and their stability in air, conventional diffraction measurements at ambient temperature in air were performed, coupled with STA either in air or inert atmosphere. These results are depicted in chapter 4. The main object of the presented thesis are high-temperature structural investigations, hence, chapter 5 is dedicated to the results of high-temperature synchrotron and neutron diffraction on powdered samples performed over a wide temperature range. Results of INS for both the non-superionic and superionic phases of AgCuSe and AgCuS are presented in chapter 6. Finally, a summary of the work and the relevance of the obtained results as a base for further experimental or theoretical investigations are summarized in chapter 7.

Chapter 2

Survey

2.1 Superionicity

A short overview of the factors promoting superionic behaviour and possible classifications of superionic conductors are given in this section. Hence, superionic conductors are those materials that allow macroscopic transport of ions through their structure, leading to exceptionally high (liquid-like) values of ionic conductivity whilst in the solid state. The superionicity typically occurs at elevated temperatures and is characterized by the rapid diffusion of a significant fraction of one of the constituent species within an essentially rigid framework formed by the other species [2]. The factors promoting superionic behaviour according to reference [1] are:

◦ Concentration of mobile ions. Increasing the concentration n of mobile ions within the expression $\sigma_i = n \cdot Z \cdot e \cdot \mu$ is clearly advantageous, provided there are a sufficient number of suitable empty sites to accommodate them.

◦ Structure of the immobile sublattice. The presence of numerous unoccupied or partially occupied interstitial sites within the immobile sublattice (for instance, the tetrahedral and octahedral sites in the superionic cubic face centered (fcc) phases of $Cu_{2-\delta}Se$, AgCuSe and AgCuS) will promote superionic behaviour, but also requires the presence of low energy pathways (conduction channels) between these sites to enhance the mobility μ.

◦ Ionic polarizability. Highly polarizable ions within the immobile sublattice can deform to allow diffusing ions to 'squeeze' through smaller gaps.

◦ Bonding character. The preferred co-ordination of a mobile ion (tetrahedral, octahedral, *etc.*) is a manifestation of the bonding character of the material. It has been suggested that mixed bonding character (such as ionic-covalent bonding like in $Cu_{2-\delta}Se$, AgCuSe, AgCuS and Ag_3CuS_2) is an essential characteristic of good superionics by allowing the mobile ion to adopt several different co-ordinations during the diffusion process.

◦ Ionic charge. Lower charge results in lower Coulomb energy barriers during diffusion.

◦ Ionic radius. Small mobile ions fit better through the gaps in the polyhedral faces formed by the immobile sublattice.

Known superionic conductors were categorized according to their technological function, the nature of the transition to the highly conducting state (abrupt or continuous), their constituent chemical species or crystal structures [1]. The classification proposed by Boyce and Huberman [9], *i. e.*, the manner in which the superionic state is achieved, should be especially denoted:

◦ Type I superionic materials are superionic at temperatures above a first-order structural phase transition. This behaviour is typified by the superionic α-phase of AgI (see [1] and references therein). In this material the ionic conductivity increases by around three orders of magnitude, on passing through the $\beta \longrightarrow \alpha$ phase transition at 420 K .

◦ Type II superionic materials attain high levels of ionic conductivity following a gradual and continuous disordering process within the same phase. Below the superionic transition, T_c, the number of conducting defects increases rapidly before saturating above T_c. The superionic transition is often accompanied by an anomaly in the specific heat and lattice expansion. β-PbF_2 displays typical type II superionic behaviour (see [1] and references therein).

◦ Type III superionic materials do not have a clear phase transition, but achieve high levels of ionic conduction *via* increased mobility of a (generally fixed) number of thermally activated defects. An Arrhenius plot of the temperature dependence of the ionic conductivity for a type III superionic conductor would show linear behaviour. Sodium β-aluminas are typical type III superionic materials (see [1] and references therein).

2.2 Ionic conductivity in copper- and silver- based selenides and sulfides

The ionic conductivity and chemical diffusion measurements on copper (I) selenide, $Cu_{2-\delta}Se$, were reported in a wide temperature range for samples with a different deviation from the stoichiometric composition δ [10,11] (see also table 2.1). The ionic conductivity was measured with the use of $Cu|CuBr{\cdot}C_6H_{12}N_4CH_3Br|Cu_{2-\delta}Se|Pt$ cells for the non-superionic α- and the superionic β-phases [10]. By sending a current through such a cell, the value of δ is changed continuously in a controlled manner. It was found that ionic conductivity decreases non-linear with an increase of δ in superionic β-$Cu_{2-\delta}Se$. Such non-linear changes in the ionic conductivity cannot be accounted by the model that a certain number of copper ions are immobile. According to [10], the reason of decrease in ionic conductivity with decreasing δ is not clear but it might be ascribed to electron-ion (hole-vacancy as in this case) interaction. On the other hand, ionic conductivity in non-superionic α-$Cu_{2-\delta}Se$ shows an increase with increasing δ. This is in contrast to the superionic β- phase and suggests that the lattice defects in the α-phase are of the Frenkel type [10].

Ionic conductivity of superionic β-$Cu_{2-\delta}Se$ was measured by using electrochemical cell $Pt|Cu|CuBr|Cu_{2-\delta}Se|CuBr|Cu|Pt$ in the range of 573-673 K for samples with δ=0-0.125 [11]. Deviation from stoichiometry was controlled by coulometric titration. It was revealed that an increase of δ leads to a decrease of ionic conductivity in agreement with [10]. On the other hand, it was supposed that $\frac{7}{8}$ of all copper are immobile in stoichiometric β-Cu_2Se and an increase of δ is related with a decrease of the portion of mobile cations whereas the number of immobile cations is constant. Hence, in contrast to [10], the change in ionic conductivity as a function of δ was explained in reference [11] by changes of the number of mobile cations.

In [12,13] was reported that special caution is necessary to the problem discriminating the conduction of Cu^+ and Ag^+ ions in $(Ag_xCu_{1-x})_2Se$ with x=0...1. Nevertheless, it was shown that the total ionic conduction of the mobile Cu^+ and Ag^+ ions can be treated as conduction of one species of ions. Hence, the total ionic conductivity of $(Ag_xCu_{1-x})_2Se$ was measured electrochemically by using galvanic cells $Ag|AgI|AgCuSe|Pt$. For AgCuSe an increase in the total ionic conductivity at the superionic phase transition by the factor of 10^2 was reported

Table 2.1: The values of the ionic conductivity for selected copper- and/or silver- based selenides and sulfides at selected temperatures.

	Temperature (K)	Ionic conductivity ($\Omega^{-1}\cdot cm^{-1}$)	Reference
Cu_2Se	413	~ 0.9	[10]
$Cu_{1.8}Se$		~ 0.7	
Cu_2Se	598	~ 1.9	[11]
	623	~ 2.1	
	673	~ 2.3	
$Cu_{1.95}Se$	598	~ 1.5	
	623	~ 1.65	
	673	~ 1.9	
$Cu_{1.85}Se$	598	~ 0.9	
	623	~ 1.0	
	673	~ 1.1	
AgCuSe	600	~ 2.8	[13]
	800	~ 3.9	
	1000	~ 5.1	
AgCuSe	500	~ 1.9	[14]
	600	~ 2.7	
$Ag_{0.6}Cu_{1.4}Se$	500	~ 1.4	
	600	~ 2.3	
$Ag_{1.2}Cu_{0.8}Se$	500	~ 2.0	
	600	~ 2.9	
$Ag_{0.4}Cu_{1.6}S$	573	~ 2.0	[15]
AgCuS		~ 2.4	
$Ag_{1.2}Cu_{0.8}S$		~ 2.6	

[13]. Furthermore, the ionic conductivity in the superionic phase of AgCuSe is large (see table 2.1) and not significantly dependent on the temperature and Ag/Cu ratio. The same conclusions on the base of total and partial Cu^+ and Ag^+ ionic conductivity measurements on Cu_2Se-Ag_2Se solid solutions were later reported in reference [14]. In this reference was further shown, that Cu_2Se-Ag_2Se solutions possess very promising thermoelectric properties, therefore, an implementation of these materials in thermoelectric devices is of considerable interest.

The values of total and partial ionic conductivity of fcc $(Ag_xCu_{1-x})_2S$ with x=0...1 were measured as a function of composition and temperature in the range of 473-673 K by using Pt|Ag|AgI|$(Ag_xCu_{1-x})_2S$|AgI|Ag|Pt electrochemical cells [15] (see table 2.1). A

moderate increase of ionic conductivity with an increase of silver content was revealed for the solid solutions on the base of the fcc structure in the 20...80 mol.% composition range. Moreover, from results presented in [15] follows that the total ionic conductivity is practically independent on temperature in the range of 473-673 K.

2.3 Crystal structures

2.3.1 Copper (I) selenide, $Cu_{2-\delta}Se$ (δ=0-0.25)

Copper (I) selenide (mineral name berzelianite), $Cu_{2-\delta}Se$ with δ=0-0.25, exists in two modifications: the low-temperature α-phase and the high-temperature superionic β-phase with high mobility of the copper cations. Note that numerous authors labelled these structural modifications *vice versa*. The equilibrium phase diagram of the Cu-Se system in the region of non-stoichiometric $Cu_{2-\delta}Se$ has been intensively investigated previously, nevertheless, principal data differ in literature. For instance, considerable differences can be seen in the room temperature (RT) homogeneity ranges of the α- and β-phases of $Cu_{2-\delta}Se$, in the temperature of the $\alpha \longrightarrow \beta$ superionic phase transition for stoichiometric Cu_2Se as well as in the lattice parameter of $Cu_{1.8}Se$ at ambient temperature (see table 2.2). It was recently suggested that such significant differences in the phase diagram can be associated with an uncertainty regarding the composition of the samples for which data are given [16].

Although the structure of the non-superionic α-phase was already investigated several times, a reinvestigation is necessary for a consistent composition and a more precise determination. Moreover, there are many noticeable contradictions in the literature concerning the crystal symmetry of stoichiometric α-Cu_2Se (see table 2.3). In several publications on "single" crystal studies [17,18] multiple twinning and smearing out of Bragg reflections in stoichiometric α-Cu_2Se was reported. It should be noted that an application of group-theoretical methods to the reduction of symmetry at the superionic $\alpha \longleftrightarrow \beta$ phase transition showed the possibility of 12 monoclinic twin orientations [19]. Furthermore, in this reference a hypothesis about an incommensurate structure was proposed for α-Cu_2Se, but this was not discernable from presented experimental data.

Table 2.2: Differences in the room temperature homogeneity ranges of α- and β-$Cu_{2-\delta}Se$, in the temperature of superionic $\alpha \longrightarrow \beta$ phase transition for Cu_2Se as well as in the lattice parameter of $Cu_{1.8}Se$ at ambient temperature. XRD – X-ray powder diffraction, EC – electrical conductivity, DTA – differential thermal analysis, Dil – dilatometry, ED – electron diffraction, DSC – differential scanning calorimetry, EPMA – electron probe microanalysis.

Homogeneity region of the α-phase at RT	Homogeneity region of the β-phase at RT	Temperature of $\beta \longrightarrow \alpha$ phase transition for Cu_2Se (K)	Lattice parameter of $Cu_{1.8}Se$ at RT (Å)	Experimental method	Reference
–	–	383	5.729	XRD	[20]
–	–	383	5.759	XRD	[21]
–	$1.75 \leq 2\text{-}\delta \leq 1.82$	–	–	DTA	[22]
$1.96 \leq 2\text{-}\delta \leq 2.00$	–	415	–	EC	[23]
–	$1.80 \leq 2\text{-}\delta \leq 1.85$	403±5	5.751	XRD	[24]
–	$1.73 \leq 2\text{-}\delta \leq 1.79$	–	–	EC	[25]
–	–	396±13	5.765	XRD + DTA	[26]
Very narrow homogeneity range	$1.750 \leq 2\text{-}\delta \leq 1.805$	413±3	5.7605(5)	XRD	[27]
–	–	413	–	Dil + EC + ED	[28]
$1.96 \leq 2\text{-}\delta \leq 1.99$	$1.75 \leq 2\text{-}\delta \leq 1.85$	413 (for $Cu_{1.99}Se$)	–	DSC	[29]
$1.965 \leq 2\text{-}\delta \leq 2.00$	–	413	–	Dil	[30]
–	$1.75 \leq 2\text{-}\delta \leq 1.80$	–	5.761	XRD + EPMA	[31]

Table 2.3: Crystallographic data for non-superionic stoichiometric α-Cu_2Se. XRSD – X-ray single crystal diffraction, XRPD – X-ray powder diffraction, ED – electron diffraction.

	Temperature (K)	Crystal system	Lattice dimensions				Experimental method	Reference
			a (Å)	b (Å)	c (Å)	β (deg.)		
Cu_2Se	298	cubic	2×(5.7 - 5.8)	–	–	–	XRSD	[20]
$Cu_{1.96}Se$	293	tetragonal	11.49	–	11.72	–	XRPD	[21]
$Cu_{1.9}Se$	363	tetragonal	4.94	–	4.90	–	XRPD	[32]
Cu_2Se	298	orthorhombic	11.704	8.273	4.198	–	XRPD	[33]
Cu_2Se	298	orthorhombic	4.118	7.032	20.381	–	XRPD	[34]
Cu_2Se	293	orthorhombic	4.118	2×7.032	20.381	–	XRPD	[24]
Cu_2Se	298	monoclinic	14.087	20.481	4.145	90.38	XRPD	[26]
Cu_2Se	298	monoclinic	12.30	12.30	40.74	120±1	ED	[28]
Cu_2Se	298	monoclinic	7.115(5)	12.34(1)	7.119(5)	108.0(4)	XRSD	[35]
Cu_2Se	298	pseudo-monoclinic	7.14	81.9	7.14	120	XRPD + XRSD + ED	[18]
Cu_2Se	300	cubic	5.694(7)	–	–	–	XRSD	[17]
Cu_2Se	298	monoclinic	7.11(1)	12.44(1)	7.13(1)	107.9(4)	XRPD	[36]
Cu_2Se	293	cubic	5.8164	–	–	–	XRPD	[37]

Table 2.4: The models for the average structure of superionic β-$Cu_{2-\delta}Se$ resulting from single crystal diffraction. Se^{2-} is situated on the 4(a) site.

Sample	Temperature (K)	Approach	Space group	Cu^+ crystallographic sites	Reference
Cu_2Se	383	harmonic thermal motion	$F23$	4(c) + 4(b) + 16(e)	[20]
Cu_2Se	433	anharmonic thermal motion	$Fm\overline{3}m$	32(f)	[38]
	483				
	633				
$Cu_2Se/Cu_{1.8}Se$	298	maximum entropy method	$Fm\overline{3}m$	8(c) + 4(b)	[39]
	433				
Cu_2Se	433	harmonic thermal motion	$Fm\overline{3}m$	8(c) + 32(f)	[17]
				8(c) + 24(e) + 32(f)	
		anharmonic thermal motion		8(c) + 24(e)	

Table 2.5: The models for the average structure of superionic β-$Cu_{2-\delta}Se$ resulting from powder diffraction. Se^{2-} is situated on the 4(a) site.

Sample	Temperature (K)	Space group	Cu^+ crystallographic sites	Reference
$Cu_{1.8}Se$	298	$F\overline{4}3m$	4(b) + 4(c) + 4(d) + 16(e)	[21]
$Cu_{1.8}Se$	298	$F\overline{4}3m$	4(b) + 4(c) + 16(e)	[24]
$Cu_{1.8}Se$	298	$Fm\overline{3}m$	8(c) + 32(f)	[40]
$Cu_{1.75}Se$	298	$Fm\overline{3}m$	8(c) + 32(f)	[36]
$Cu_{1.75}Se$	298	$Fm\overline{3}m$	8(c) + 32(f)	[37]

Superionic β-$Cu_{2-\delta}Se$ is characterized by structural disorder. Its knowledge is necessary for a description of possible copper jumps between available lattice sites within the rigid fcc selenium cage. This cation jumping is the main mechanism of the high ionic conductivity. In the view of the antifluorite structure type (adopted by superionic β-$Cu_{2-\delta}Se$ with δ = 0 - 0.25, α-AgCuSe, δ-AgCuS and δ-Ag_3CuS_2), the most probable mechanism for cation motion is from the tetrahedral through the octahedral to another tetrahedral void within the fcc anion cage. Up to now the structure properties of superionic β-$Cu_{2-\delta}Se$ have been investigated by elastic coherent (Bragg) scattering, and a set of different models for structural disorder has been proposed (see tables 2.4 and 2.5).

Thus, the average structures of stoichiometric Cu_2Se [17,20,38,39] and non-stoichiometric $Cu_{1.8}Se$ [39] in the superionic β-phase were described by single crystal diffraction. One of the earliest paper on the high-temperature structure of Cu_2Se (383 K) by Rahlfs [20] reports that the 4(c) site is fully occupied by 4 Cu^+ ions and the other 4 Cu^+ ions are statistically distributed between 4(b) and 16(e) sites within the fcc selenium in 4(a) at (0, 0, 0) cage (space group $F23$). In reference [38] results of single crystal neutron diffraction on β-Cu_2Se are presented. Only one equilibrium position for Cu^+ ions on a 32(f) site at (x, x, x) with $\frac{1}{4} \leq x \leq \frac{1}{3}$ was found in space group $Fm\overline{3}m$ sufficient to describe the structure at 433, 483 and 633 K. Hence, no significant electron density was revealed on the ideal octahedral site 4(b) at ($\frac{1}{2}$, $\frac{1}{2}$, $\frac{1}{2}$) and it was suggested that copper ions jumps will therefore require a high activation energy [38]. On the other hand, the results from this reference might be questioned due to the analysis with an anharmonic description of thermal motion, although only 33-34 Bragg maxima were collected. In the reference [17] two different analyses with implementation of harmonic and anharmonic thermal motion approaches were composed for the data collected at 433 K from a Cu_2Se single crystal. It is very important to underline that harmonic modelling (Cu^+ ions were distributed between two 8(c) at ($\frac{1}{4}$, $\frac{1}{4}$, $\frac{1}{4}$) and 32(f) at (x, x, x) with $\frac{1}{4} \leq x \leq \frac{1}{3}$ sites as well as between three 8(c) at ($\frac{1}{4}$, $\frac{1}{4}$, $\frac{1}{4}$), 24(e) at ($\frac{1}{2}$, 0, 0) and 32(f) at (x, x, x) with $\frac{1}{4} \leq x \leq \frac{1}{3}$ sites, $Fm\overline{3}m$) gave the same (and/or lesser) quality of fit as an anharmonic model with more parameters (Cu^+ ions distributed over 8(c) at ($\frac{1}{4}$, $\frac{1}{4}$, $\frac{1}{4}$) and 24(e) at ($\frac{1}{2}$, 0, 0) sites, $Fm\overline{3}m$) [17]. The X-ray single crystal diffraction investigation of the cation distribution in Cu_2Se and $Cu_{1.8}Se$ at 291 and 433 K by the maximum entropy

method is reported in [39]. It was concluded that copper ions tend to occupy the ideal tetrahedral 8(c) at ($\frac{1}{4}$, $\frac{1}{4}$, $\frac{1}{4}$) and the ideal octahedral 4(b) at ($\frac{1}{2}$, $\frac{1}{2}$, $\frac{1}{2}$) sites. In this work was also denoted that the observed Bragg reflections from the samples had smeared tails because of imperfections of the single crystals.

The models for the average structures of the superionic stoichiometric and non - stoichiometric copper (I) selenide as results of X-ray powder diffraction investigations are reported in several references [21, 24, 26, 27, 36, 37, 40]. The atomic arrangement in the fcc β-$Cu_{2-\delta}Se$ was described by Borchert [21] in the following way: anions are on 4(a) at (0, 0, 0) sites while cations are distributed over the 4(b) at ($\frac{1}{2}$, $\frac{1}{2}$, $\frac{1}{2}$), 4(c) at ($\frac{1}{4}$, $\frac{1}{4}$, $\frac{1}{4}$), 4(d) at ($\frac{3}{4}$, $\frac{3}{4}$, $\frac{3}{4}$) and a 16(e) site at (x, x, x) with $x = \frac{2}{3}$ within $F\overline{4}3m$ symmetry. In this reference was also reported that thermal expansion coefficient of β-$Cu_{1.8}Se$ decreases with temperature increase up to 523 K and becomes linear above 523 K. This phenomenon was explained by changes in the distribution of the mobile copper in fcc selenium cage. In contrast to [21], no Cu^+ on the 4(d) site and $x = 0.71$ was proposed for $Cu_{1.8}Se$ in reference [24]. In the work of Tonejc *et al.* [27] high-temperature powder diffraction in Debye-Scherrer mode was performed on β-$Cu_{2-\delta}Se$ with $1.72 \leq 2\text{-}\delta \leq 1.86$ in the temperature range 298-609 K. The "unusual" behaviour of thermal expansion in superionic copper selenide up to 523 K was attributed to the temperature induced cation redistribution in the structure with no further change above 523 K. The redistribution of cations with temperature up to 523 K is supposed by changes in the intensities of specific diffraction lines [21, 27]. In reference [40] a model for the average structure of $Cu_{1.8}Se$ was proposed based on space group $Fm\overline{3}m$: 5.2 cations are situated on the tetrahedral 8(c) site at ($\frac{1}{4}$, $\frac{1}{4}$, $\frac{1}{4}$) and 2 on the trigonal 32(f) site at (x, x, x) with $x = \frac{1}{3}$. In the works of Danilkin *et al.* [36] and Machado *et al.* [37] the RT structural investigations were performed on powdered samples with stoichiometry $Cu_{1.75}Se$ and $Cu_{1.8}Se$. According to Danilkin *et al.* [36] the cations are distributed over the tetrahedral 8(c) site at ($\frac{1}{4}$, $\frac{1}{4}$, $\frac{1}{4}$) and an octahedral 32(f) site at (x, x, x) with $x = 0.400$ (space group $Fm\overline{3}m$ symmetry). Machado *et al.* [37] informed that cations are distributed over tetrahedral 8(c) at ($\frac{1}{4}$, $\frac{1}{4}$, $\frac{1}{4}$) and trigonal 32(f) at (x, x, x) with $x = \frac{1}{3}$ sites (space group $Fm\overline{3}m$ symmetry). A significant cation occupation of 32(f) sites has been underlined in the last two publications.

2.3.2 Silver copper (I) selenide, AgCuSe

Table 2.6: Crystallographic data on the crystalline system of the non-superionic β-AgCuSe. XRPD – X-ray powder diffraction, ED – electron diffraction.

Crystalline system, Symmetry	Lattice dimensions			Experimental method	Reference
	a (Å)	b (Å)	c (Å)		
tetragonal, $P4/nmm$	4.075	–	6.29	XRPD	[41]
orthorhombic, $Pmmn$	4.105	20.35	6.31	XRPD	[42]
orthorhombic, $Pmmn$	4.105	20.35	6.31	ED	[43]
tetragonal, $P4/nmm$	4.083	–	6.30	XRPD	[44, 45]
orthorhombic, $Pmmn$	4.121	20.41	6.326	XRPD	[46]
orthorhombic, $Pmmn$	4.105	40.07	12.620	ED	[47]
orthorhombic, $Pmmn$	4.105	40.07	12.620	XRPD	[48]

The earliest structural investigation revealed a tetragonal structure of silver copper (I) selenide AgCuSe (mineral name eucairite) at RT, space group $P4/nmm$, with lattice parameters $a = 4.075$, $c = 6.29$ Å and Z=2 [41]. Shortly thereafter, Frueh [42] showed that AgCuSe at RT (β-phase) crystallizes in pseudo-tetragonal orthorhombic symmetry and has a large supercell $a\times5a\times c$ with $Z = 10$ (space group $Pmmn$) based on the previously reported tetragonal subcell with a between 4.07 and 4.105 Å and $c = 6.31$ Å. The existence of a reversible phase transition into the high-temperature phase (α) at 463-468 K was also mentioned for the first time. During investigations of the structural transitions in copper- and silver- based chalcogenides, Kiazimov *et al.* found the equilibrium temperature between the low- (β) and high-temperature (α) modifications of AgCuSe equal to 504 K, *i.e.* only the cubic phase is present above this temperature [44, 45]. In these works high temperature AgCuSe was indexed based on fcc cell with $a = 6.080$ Å at 523 K. Recently, in the reference [46] some "extra" reflections in the diffraction pattern of non-superionic β-AgCuSe at RT were detected, which were not listed in the previous literature. In the next structural work on β-AgCuSe a large superstructural orthorhombic cell was proposed on the base of electron diffraction measurements [47]. In this recent work diffraction patterns of β-AgCuSe at RT were indexed based on an orthorhombic cell $a\times10a'\times2c$ with Z=40, where $a = 4.105$

Å, $a' = 4.070$ Å and $c = 6.310$ Å are the lattice parameters of the basic tetragonal (or rather orthorhombic) primitive subcell proposed in [42]. The pronounced structural disordering in superionic α-AgCuSe was mentioned in [49]. In this communication the structure was characterized only at 523 K by conventional X-ray powder diffraction: anions are situated on the 4(a) site at (0, 0, 0), whereas cations are statistically distributed on 8(c) at $(\frac{1}{4}, \frac{1}{4}, \frac{1}{4})$ and 32(f) at (x, x, x) with $\frac{1}{3} < x < \frac{1}{2}$ (space group $Fm\overline{3}m$).

2.3.3 Silver copper (I) sulfide, AgCuS

The earliest structural investigations reported an orthorhombic structure for silver copper (I) sulfide AgCuS (mineral name stromeyerite) at RT, either with space group $Cmc2_1$ or $Cmcm$ [52] or $Cmcm$ [53] with lattice parameters a=4.06 Å, b=6.66 Å, c=7.99 Å and Z=4. In these works the RT structure was described as zigzag chains of silver and sulfur atoms parallel to the c axis, the planes parallel to (001) are composed of loosely packed face-centered layers of silver atoms alternating with layers of triangularly coordinated sulfur and copper atoms [52, 53]. Moreover, a pseudo-hexagonal symmetry of the RT stromeyerite structure was mentioned in [53]. Shortly thereafter, phase relations in the Cu–Ag–S system were studied by Djurle [54] and Skinner [55]. Djurle investigated AgCuS by powder X-ray diffraction at four temperature points and reported on the existence of high-temperature hexagonal and cubic modifications together with their approximated stability ranges phases: orthorhombic, hexagonal and cubic phases exist at RT-363 K, 363 - 453 K and above 453 K, respectively [54]. The work of Skinner [55] was guided by a mineralogical interest in stromeyerite. The following phase transitions of stromeyerite at elevated temperatures have been found: orthorhombic $\stackrel{366K}{\longrightarrow}$ hexagonal $\stackrel{400K}{\longrightarrow}$ hexagonal+cubic $\stackrel{438K}{\longrightarrow}$ cubic.

AgCuS was studied by powder and single crystal diffraction techniques in the more recent investigations of Skarda *et al.* [51] and Baker *et al.* [50], respectively. Neutron powder diffraction at four selected temperatures (RT, 373, 388 and 523 K) revealed hexagonal and cubic phases of AgCuS. It was mentioned that the highly disordered hexagonal phase gave a very weak diffraction pattern with seven Bragg reflections. The structure of hexagonal AgCuS is isostructural to Cu_2S and was refined in space group $P6_3/mmc$ with lattice parameters a=4.1389(10) Å and c=7.0817(27) Å, Z=2 at 388 K: anions were situated on the

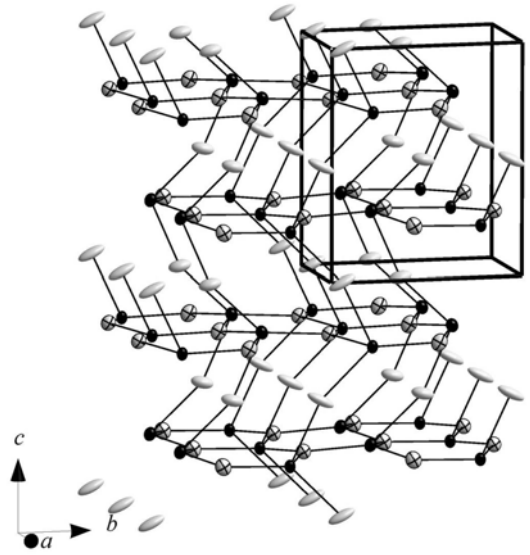

(a) AgCuS at 120 K ($Pmc2_1$) [50]

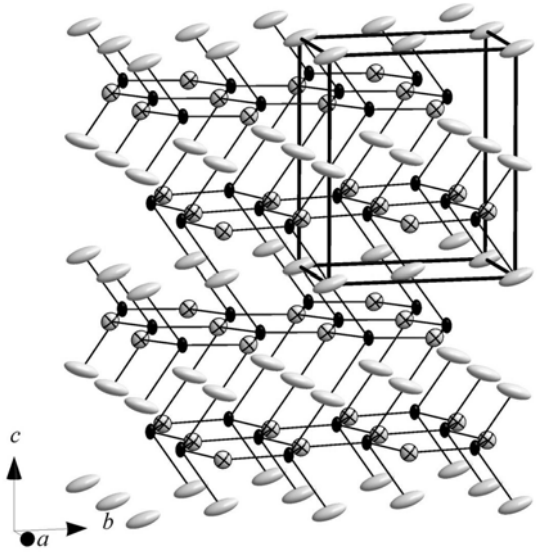

(b) AgCuS at RT ($Cmc2_1$) [50]

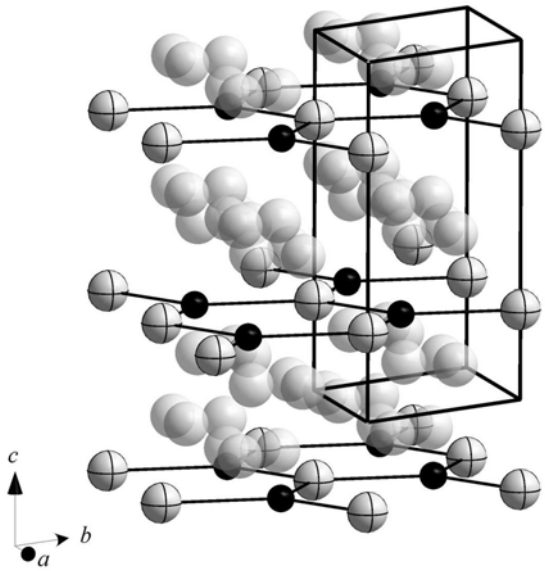

(c) AgCuS at 380 K ($P6_3/mmc$) [51]

Figure 2.1: The crystal structures of orthorhombic and hexagonal stromeyerite. In plots (a) and (b) black, grey and grey with inner lines ellipsoids illustrate sulphur, silver and copper, respectively. Plot (c) represents a ball-stick representation of hexagonal AgCuS (sulphur in black, silver plus copper in grey and copper ions in grey with inner lines.

2(d) site and cations on a 12(k) site, partial population of 2(b) site solely by copper cations was indicated as well (see figure 2.1 and table 2.7). AgCuS at RT was refined in space group *Cmcm* (see table 2.7), and a cubic phase of AgCuS at higher temperatures was mentioned but not specified by Skarda *et al.* [51]. The RT space group of stromeyerite has been precessionally determined by single crystal X-ray diffraction in combination with convergent-beam electron diffraction to be $Cmc2_1$ in the newest work on the structure of AgCuS by Baker *et al.* [50] (see figure 2.1 and table 2.8). Primary structural features are the same as those proposed in [52, 53], the structure is non-centrosymmetric and polar in *c*-direction with a large and highly anisotropic thermal motion of silver ions. Distorted sulphur hexagonal close packing (hcp) was mentioned as well. Moreover, single crystal diffraction data for AgCuS were collected at 120 and 13 K and it was found that the symmetry of stromeyerite decreases from $Cmc2_1$ to its maximal non-isomorphic subgroup $Pmc2_1$ at low-temperatures [50] (see figure 2.1 and table 2.8). This order-disorder transition is reversible and of second-order. The transition temperature was estimated to 250 K [50].

Table 2.7: Structural parameters of AgCuS according to reference [51].

Space group	*Cmcm*			*Cmcm*			$P6_3/mmc$		
Temperature (K)	298			323			380		
a (Å), b (Å), c (Å)	4.0638(4)	6.6337(6)	7.9724(7)	4.0672(3)	6.6392(5)	7.9681(6)	4.1389(10)	–	7.0817(27)
Z	4			4			2		
S, site	4(c)			4(c)			2(d)		
x, y, z	$\frac{1}{4}$	0.7837(11)	$\frac{1}{4}$	0	0.7861(9)	$\frac{1}{4}$	$\frac{1}{3}$	$\frac{2}{3}$	$\frac{3}{4}$
B_{iso} (Å^2)	1.48(24)			1.99(17)			3.26(1.28)		
Occupancy	1			1			1		
Ag, site	4(a)			4(a)			12(k)		
x, y, z	0	0	0	0	0	0	0.2573	0.5146	0.4339
B_{iso} (Å^2)	5.59(16)			6.48(15)			8.61(1.39)		
Occupancy	1			1			0.1667		
Cu, site	4(c)			4(c)			12(k)		
x, y, z	0	0.4311(5)	$\frac{1}{4}$	0	0.4324(4)	$\frac{1}{4}$	0.2573	0.5146	0.4339
B_{iso} (Å^2)	2.15(10)			2.56(8)			8.61(1.39)		
Occupancy	1			1			0.04887		
Cu1, site							2(b)		
x, y, z							0	0	$\frac{1}{4}$
B_{iso} (Å^2)							12.03(1.61)		
Occupancy							0.7068		
R_{Bragg}, R_{wp}, R_E	0.0947	0.0777	0.0635	0.1003	0.0758	0.0589	0.2285	0.0930	0.0784

Table 2.8: Structural parameters of AgCuS according to reference [50] (ICSD cards 66580 and 66581). u_{ij} have been multiplied by 100.

Space group	$Cmc2_1$				$Pmc2_1$			
Temperature (K)	298				120			
a (Å), b (Å), c (Å), Z	4.059(2)	6.617(4)	7.967(2)	4	4.0470(4)	6.5920(7)	7.9300(8)	4
S1, site		4(a)				2(a)		
x, y, z	$\frac{1}{2}$	0.2859(6)	0.2484(15)		1	0.2161(4)	0.7215(5)	
u_{11} (Å^2), u_{22} (Å^2), u_{33} (Å^2)	1.35(12)	1.56(14)	3.2(2)		0.38(8)	0.58(8)	0.85(12)	
u_{12} (Å^2), u_{13} (Å^2), u_{23} (Å^2)	0	0	-0.0(3)		0	0	0.02(9)	
Occupancy		1				1		
Ag1, site		4(a)				2(a)		
x, y, z	$\frac{1}{2}$	0.495(2)	$\frac{1}{2}$		1	-0.0560(2)	$\frac{1}{2}$	
u_{11} (Å^2), u_{22} (Å^2), u_{33} (Å^2)	3.6(8)	14.4(3)	3.61(9)		1.03(3)	3.22(5)	1.17(5)	
u_{12} (Å^2), u_{13} (Å^2), u_{23} (Å^2)	0	0	-4.83(12)		0	0	-1.38(4)	
Occupancy		1				1		
Cu1, site		4(a)				2(a)		
x, y, z	0	0.4328(3)	0.2486(11)		1	0.5674(2)	0.7297(3)	
u_{11} (Å^2), u_{22} (Å^2), u_{33} (Å^2)	1.57(8)	3.14(12)	3.33(12)		0.55(5)	1.07(5)	1.22(8)	
u_{12} (Å^2), u_{13} (Å^2), u_{23} (Å^2)	0	0	-1.0(2)		0	0	0.13(6)	
Occupancy		1				1		
S2, site						2(b)		
x, y, z					$\frac{1}{2}$	0.7133(4)	0.7594(5)	
u_{11} (Å^2), u_{22} (Å^2), u_{33} (Å^2)					0.56(9)	0.73(8)	0.92(13)	
u_{12} (Å^2), u_{13} (Å^2), u_{23} (Å^2)					0	0	-0.09(9)	
Occupancy						1		
Ag2, site						2(b)		
x, y, z					$\frac{1}{2}$	0.4402(2)	0.9728(1)	
u_{11} (Å^2), u_{22} (Å^2), u_{33} (Å^2)					1.38(4)	2.33(4)	0.77(4)	
u_{12} (Å^2), u_{13} (Å^2), u_{23} (Å^2)					0	0	0.37(4)	
Occupancy						1		
Cu2, site						2(b)		
x, y, z					$\frac{1}{2}$	0.0663(2)	0.7424(3)	
u_{11} (Å^2), u_{22} (Å^2), u_{33} (Å^2)					0.58(5)	0.88(5)	0.94(8)	
u_{12} (Å^2), u_{13} (Å^2), u_{23} (Å^2)					0	0	0.06(6)	
Occupancy						1		
R, wR	0.061	0.059			0.036	0.033		

2.3.4 Trisilver copper (I) sulfide, Ag_3CuS_2

The compound trisilver copper (I) sulfide, Ag_3CuS_2, found in nature as the mineral jalpaite, exists as a discrete phase on the pseudo-binary tie line between Ag_2S (acanthite) and Cu_2S (chalcocite) [56]. The RT diffraction pattern from jalpaite was indexed based on a tetragonal body-centered (bcc) unit cell [54], moreover, the following sequence of high-temperature phase transitions was revealed in this work: tetragonal $\overset{385K}{\longrightarrow}$ cubic (bcc) $\overset{563-583K}{\longrightarrow}$ cubic (fcc). The fact that the *a*-axis expands and the *c*-axis contracts on heating was also mentioned, nevertheless, this suggestion was limited by the available experimental data. Shortly thereafter, the Ag-Cu-S system was studied by Skinner [55]. The following scheme for the phase transformation was revealed in this work: tetragonal $\overset{390\pm2K}{\longrightarrow}$ cubic (bcc) $\overset{?}{\longrightarrow}$ cubic (bcc) plus cubic (fcc) $\overset{578\pm10K}{\longrightarrow}$ cubic (fcc).

The crystal structure of Ag_3CuS_2 has been determined by X-ray powder diffraction in the work of Baker *et al.* [56] (see table 2.9 and figure 2.2). The structure exhibits a distorted bcc sulphur packing and two distinct silver sites. On one site the silver atoms are surrounded by six sulphur atoms forming a (2-4) distorted octahedral environment, whereas on the other site the silver atoms are in a distorted tetrahedral environment with two closer and two farer sulphur atoms. Copper is linearly coordinated by two sulphur atoms.

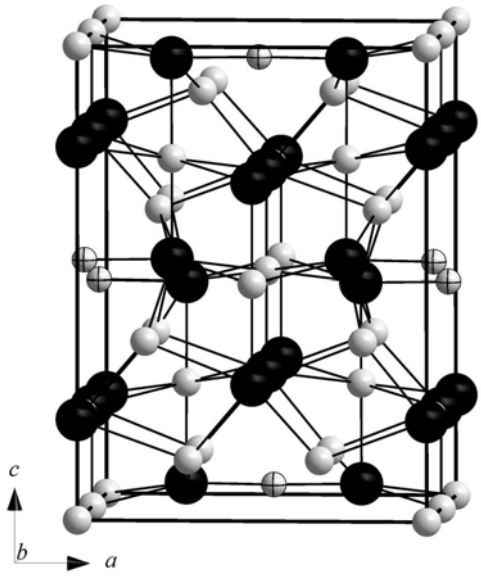

Figure 2.2: Projection of the Ag_3CuS_2 structure at RT viewed from close to [010]: black, grey and grey with inner lines ellipsoids – sulphur, silver and copper, respectively.

Table 2.9: Structural parameters of Ag_3CuS_2 according to reference [56] (ICSD card 67526).

Space group	$I4_1/amd$		
Temperature, K		298	
a (Å), c (Å)	8.6705(10)		11.7573(18)
Z		8	
Ag1, site		8(c)	
x, y, z	0	0	0
B_{iso} (Å^2)		1.9(3)	
Occupancy		1	
Ag2, site		16(g)	
x, y, z	-0.3119(3)	-0.0619(3)	0.875
B_{iso} (Å^2)		1.7(2)	
Occupancy		1	
Cu, site		8(e)	
x, y, z	0	$\frac{1}{4}$	0.5347(6)
B_{iso} (Å^2)		0.5(3)	
Occupancy		1	
S, site		16(h)	
x, y, z	0	-0.001(1)	0.2125(8)
B_{iso} (Å^2)		0.0(4)	
Occupancy		1	
R_{Bragg}, R_{wp}, R_p	0.0289	0.0563	0.0437

2.4 Motivation and open questions

For a long time copper- and silver- based halides and chalcogenides attract the attention of scientists due to their exceptional physical properties. $Cu_{2-\delta}Se$ (δ = 0, 0.15, 0.25), AgCuSe, AgCuS and Ag_3CuS_2 are important members of the family of copper- and silver- based superionic conductors. These materials in the superionic phases adopt an ionic conductivity as high as 1 $\Omega^{-1}\cdot cm^{-1}$ [10–15]. Moreover, implementation of AgCuSe in thermoelectric devices is of considerable interest [14]. In spite of these facts, high-temperature crystal structural behaviour, phase transformations and thermal expansion of the above mentioned compounds were insufficiently investigated.

In particular, the high-temperature behaviour and the influence of stoichiometry on the structure of β-$Cu_{2-\delta}Se$ were not yet considered in detail. Most results reported previously consider only specific samples with particular stoichiometry and at selected temperatures. Moreover, discrepancies in the structure of $Cu_{2-\delta}Se$ with δ = 0-0.25 result from a lack of a comprehensive and sophisticated study. Hence, structural studies on β-$Cu_{2-\delta}Se$ with dif-

ferent δ were performed over a broad range of temperatures in order to clarify the correct structure from the variety of literature reports and to elucidate the high-temperature structural behaviour (these results are described in the present thesis and also published in [57]).

The crystal structure of AgCuSe was studied only at particular temperatures, the highest one was around ∼523 K. No experimental data regarding thermal expansion, phase transitions and average structural behaviour of superionic α-AgCuSe in a wider high temperature range were found in literature. Despite of the number of structural investigations on AgCuS in literature, no information on the high-temperature thermal expansion and structural behavior within the superionic state was found. From the results of [51, 54, 55] follows that the cubic high-temperature modification of AgCuS was not yet considered. In addition, a more accurate powder diffraction study of AgCuSe and AgCuS is important as a base for both successive theoretical and experimental investigations of these highly-disordered systems. Therefore, high-temperature investigations of AgCuS and AgCuSe were performed *in situ* over a wide temperature range between RT and the melting points by synchrotron and neutron powder diffraction [48, 58]. Results of inelastic neutron scattering experiments on the superionic and the non-superionic phases of AgCuSe and AgCuS are also presented in this thesis (see also our publications [48, 59]). To our knowledge, lattice dynamics in these specific samples was studied for the first time. The main results from such measurements are experimental information regarding the vibrational density of states in the different phases of AgCuSe and AgCuS.

No information about the structural evolution in the superionic state nor about high-temperature thermal expansion of Ag_3CuS_2 were found in the literature. In order to characterize high-temperature phase transitions in Ag_3CuS_2 more precisely and to obtain valuable information about high-temperature thermal expansion, powder diffraction data were collected.

Note that the thermodynamical stability of the samples is of primary importance, because decomposition of the sample at high-temperature can seriously jeopardize the conclusions drawn from diffraction and inelastic neutron scattering. Therefore, special attention was paid to check the stability of the samples at high temperatures.

Chapter 3

Experimental

3.1 Syntheses, preliminary X-ray diffraction and simultaneous thermal analysis

All samples for powder diffraction and inelastic neutron scattering investigations were prepared *via* solid-state routes. High purity copper, silver, sulphur and selenium powders (Chempur, 99.99 %) were used for the syntheses. Powders were weighed in appropriate ratios, ground under acetone and pressed in pellets. The pellets were sealed in silica tubes at 10^{-3} mbar pressure and heated at different temperatures (about 720 K for $Cu_{2-\delta}Se$ and above 1100 K for AgCuSe, AgCuS and Ag_3CuS_2) over 50 hours with subsequent cooling down to RT in 12-24 hours. All silver containing samples were remelted at the chosen temperature and appeared homogeneous, whereas the samples without silver were additionally homogenized (*i. e.*, they were reground, pressed in pellets, sealed in silica tubes under vacuum and additionally annealed at about 573 K for 48 hours).

Conventional X-ray diffraction data for phase analyses were collected using a Stoe STADI/P powder diffractometer equipped with a position sensitive counter at wave lengths of 1.54056 Å (CuKα_1 radiation) or 0.70930 Å (MoKα_1 radiation). All conventional X-ray diffraction measurements were performed in ω-2θ geometry (transmission mode).

In order to characterize the stability of the samples, investigations *via* simultaneous thermal analysis (STA), which combined thermogravimetry (TG) and differential scanning calorimetry (DSC), were carried out on a Netzsch STA 429 device at a heating-cooling rate

of 10 K/min, either in air (for $Cu_{2-\delta}Se$ with $\delta = 0$, 0.15, 0.25, AgCuSe and AgCuS) or in argon (for $Cu_{2-\delta}Se$ with $\delta = 0$ and 0.25, AgCuSe and AgCuS).

3.2 Synchrotron and neutron powder diffraction

The high-temperature diffraction measurements [60–64] were performed at the powder diffractometer B2 which is situated at a bending magnet of the storage ring DORIS-III (Hasylab/DESY, Hamburg). This beamline is described by Knapp *et al.* [65] and shown schematically in figure 3.1. The direct unmirrored beam was used in the experiments. A Si(111) double-crystal monochromator was used for wave length selection. Three slit systems were used for beam conditioning: slit 1 in front of the mirror, slit 2 behind the monochromator and slit 3 near the sample. The primary beam was cut by slit 1 to the size of the monochromating crystals, which reduced the background level. The beam size at the sample position was adjusted by slit 2, and the optimum setting was obtained when the beam covers all of the capillary (0.3 mm). Slit 3 cuts off the radiation from the scattering at slit 2. The samples were ground in an agate mortar, filled in quartz capillaries in air ($Cu_{2-\delta}Se$ with δ=0, 0.15, 0.25) or in a glove-box (AgCuSe, AgCuS and Ag_3CuS_2) and sealed. A capillary furnace from Stoe & Cie (type 0.65.3, Debye-Scherrer geometry) was used for the temperature conditioning. In this furnace the filled capillary was placed inside a drill hole in a graphite heating element. The capillary is then rotated by a rotating disc attached to the filling funnel of the capillary. The temperature was measured *via* EUROTHERM controller. The high-temperature data were collected with the on-site readable image-plate detector OBI [66]. Additional patterns at RT were also taken after the heat treatment of the samples. A single counter consisting of a NaI scintillator with embedded photomultiplier and optional slits, parallel foils and Ge (111) analyser crystal in front was used for data collection from $Cu_{1.75}Se$ (in order to save beam time only selected 2θ-ranges were measured). Moreover, this detector system was used for the wave length determination from the positions of 10 reflections from LaB_6 reference material (SRM 660a from National Institute of Standards and Technology). A short overview of the experimental conditions is presented in table 3.1.

Complementary high-temperature neutron diffraction data were collected at the research neutron reactor FRM-II (Garching near Munich, Germany) at the structure powder diffrac-

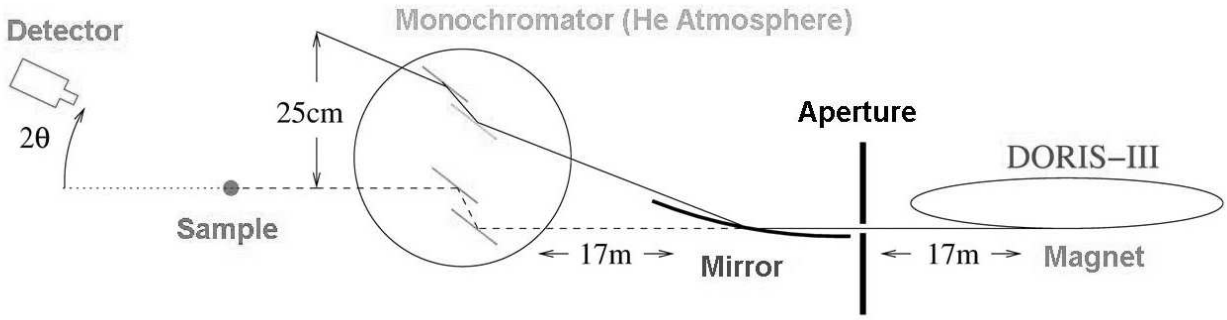

(a)

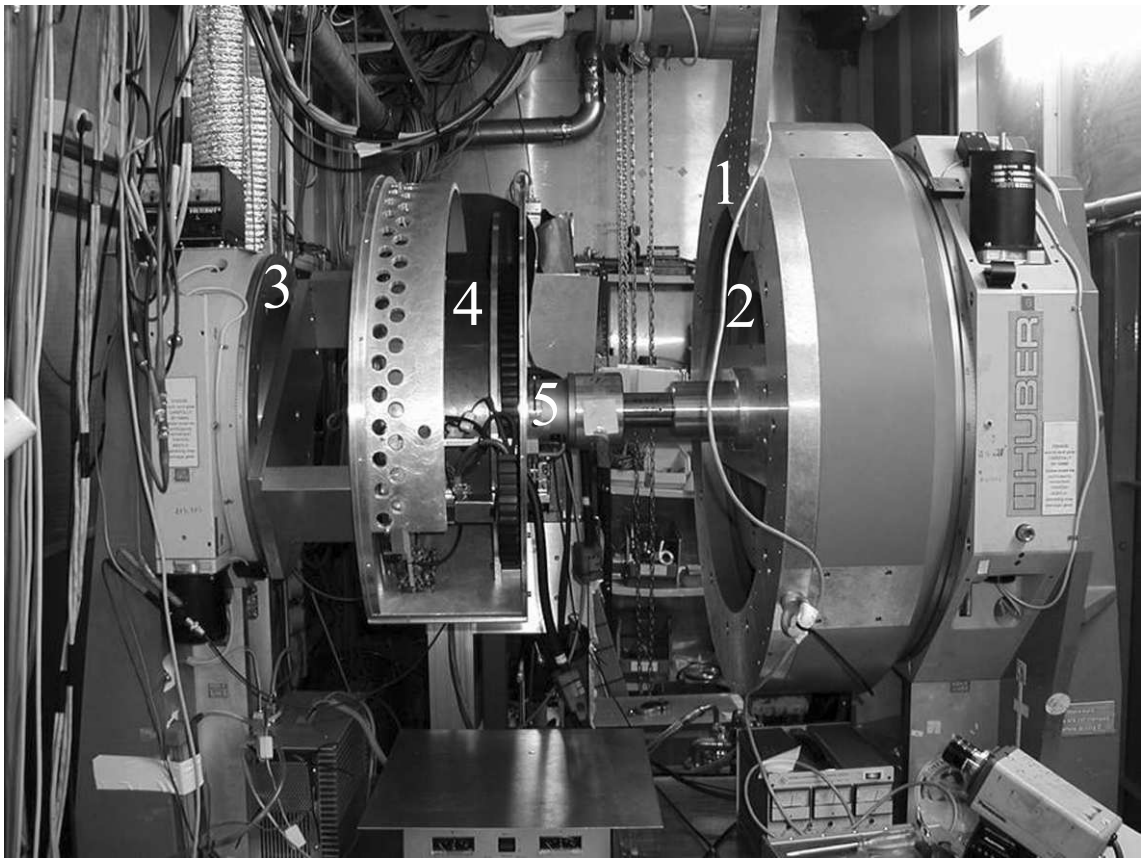

(b)

Figure 3.1: (a) – schematic representation of the beamline B2 at Hasylab/DESY, Hamburg. (b) – view of the high-resolution diffractometer B2. The synchrotron beam enters the hutch from the back. The monochromator vessel is behind the diffractometer inside the hutch. 1 – Huber circle 480 carrying the single counter; 2 and 3 – Huber circles 440 for sample environments or IP detector, respectively; 4 – image-plate detector; 5 – Stoe furnace.

tometer SPODI [67] (see figure 3.2). The samples were ground in an agate mortar. The powdered sample was then filled into a cylindrical can of 8 mm diameter made from thin (0.1 mm) niobium foil and mounted in a high-temperature vacuum furnace equipped with a Nb heating element. The temperature has been measured by a W/Re thermocouple and controlled with a EUROTHERM device. A monochromator take-off angle of 155^o was selected for the vertically focusing composite monochromator and the wavelength has been determined to 1.5487 Å by Rietveld refinement of a diffraction pattern of the silicon reference material (SRM 640b from the National Institute of Standards and Technology). Full patterns were collected over a 2θ range of 8-160^o with a step size of 0.05^o at selected temperatures for AgCuSe and AgCuS samples (see also table 3.1).

Data evaluation was performed using the package "FullProf" [68]: lattice parameters, zero shift, background (linear interpolation between selected data points in non-overlapping regions) and profile shape parameters (Caglioti) were refined by a structure independent full pattern decomposition procedure (Le Bail method); the averaged structure was then analyzed by the full-profile Rietveld method. The Le Bail method as well as Rietveld refinement are well described elsewhere [69–71] and, therefore, not repeated here.

In order to elucidate the nature of the peak broadening in $Cu_{1.75}Se$ on the basis of a simple Williamson-Hall approach (very powerful example of a possible variant of this analysis can be found in [72]), the single peak profiles were also fitted by using the "cmpr" program [73].

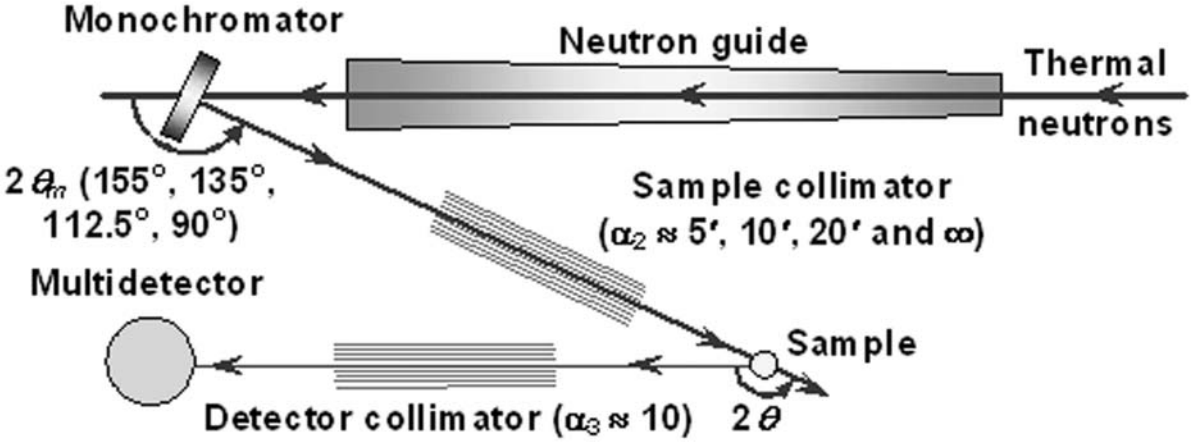

(a)

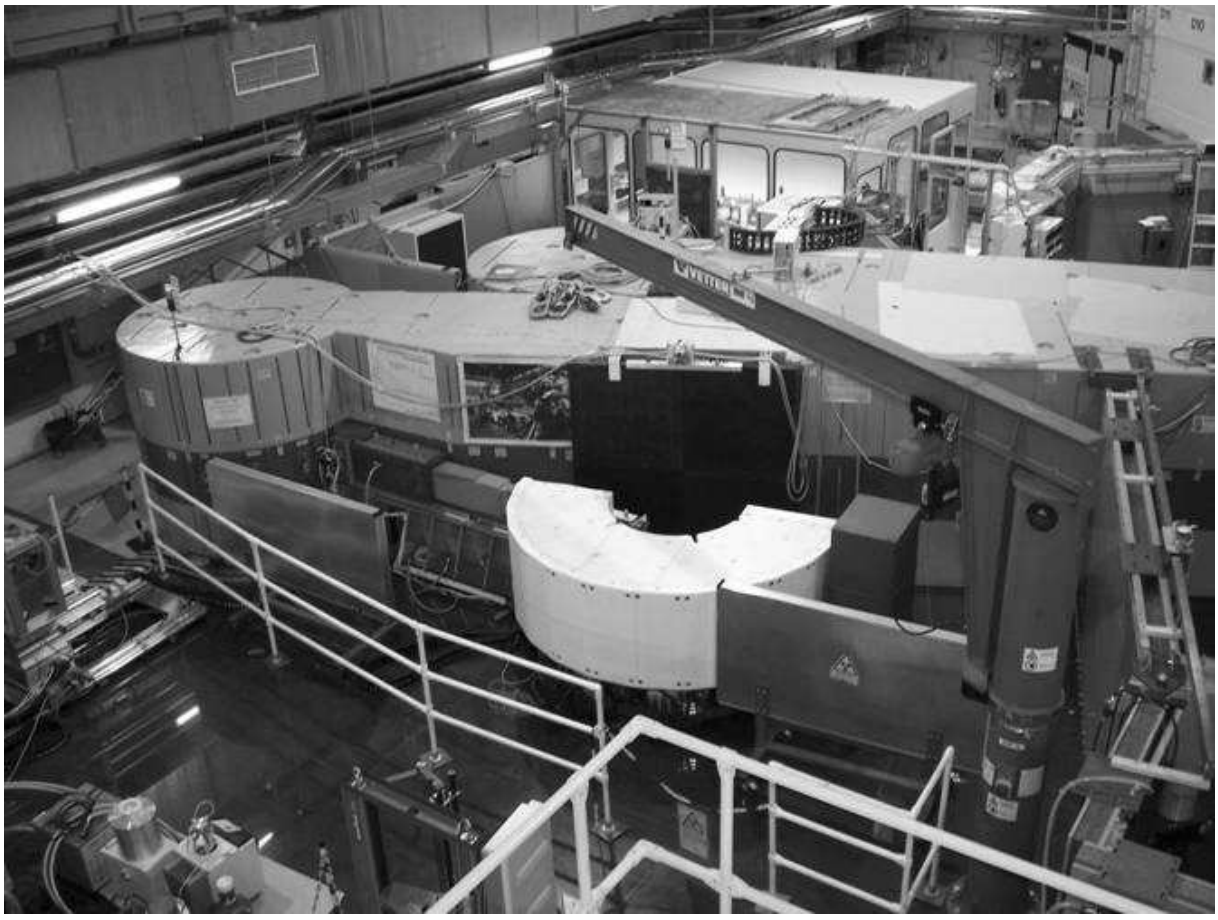

(b)

Figure 3.2: Neutron beam path (a) and view on the structure powder diffractometer SPODI (b) at FRM-II, Garching near Munich.

Table 3.1: Short overview of the experimental conditions for synchrotron and neutron diffraction measurements.

Sample	Diffractomer	Detector	Wave length (Å)	Atmosphere	Temperature range (K)	Nunber of diffraction patterns measured	2θ (deg.)	$\Delta 2\theta$ (deg.)
$Cu_{1.75}Se$	B2	image-plate	0.49993	air	RT-623	5	6 – 37	0.004
$Cu_{1.75}Se$	B2	NaI scintillator	0.50970	air	RT-573	13	8.5 – 25	0.004
$Cu_{1.85}Se$	B2	image-plate	0.49993	air	RT-613	17	6 – 37	0.004
Cu_2Se	B2	image-plate	0.49993	air	RT-623	17	6 – 37	0.004
AgCuSe	B2	image-plate	0.47001	argon	RT-973	15	4 – 40	0.004
	SPODI	80 He^3 detectors	1.5487	vacuum	RT-773	3	7 – 155	0.05
AgCuS	B2	image-plate	0.49962	argon	RT-693	26	4 –45	0.004
	SPODI	80 He^3 detectors	1.5487	vacuum	RT-873	7	7 – 155	0.05
Ag_3CuS_2	B2	image-plate	0.64071	argon	RT-1023	27	5 – 50	0.004

3.3 Inelastic neutron scattering

The INS spectra of non-superionic orthorhombic β- and superionic cubic α-AgCuSe were collected at 285 and 505 K with the DIN-2PI direct geometry spectrometer installed at the IBR-II pulsed neutron reactor in Dubna, Russia [74] (see figure 3.3). In order to reduce sample absorption and extend the kinematical range an incident neutron energy of E_0 = 18.496 meV was selected. A polycrystalline sample (about 30 g) was placed in the slab sample holder ($1 \times 5 \times 110$ mm^3) made from thin aluminium foil and mounted in a sample chamber at an angle of 60^o between the incident beam and the normal of the slab (reflection geometry). The sample chamber was evacuated down to 10^{-2} mbar. Neutron scattering data was collected simultaneously by 12 detectors at constant scattering angles Θ in the range $28^o<\Theta<134^o$. This covers the kinematical range $Q(E_0)$ from 1.94 Å^{-1} to 5.50 Å^{-1} and energy transfers $\varepsilon=E-E_0$ between -13 (negative values correspond to neutron energy loss) and 120 meV (neutron energy gain). The INS data of non-superionic orthorhombic (at 298 and 348 K) and superionic hexagonal AgCuS (at 398 K) were collected with the same spectrometer, but with slightly different experimental conditions. An incident energy of 11.8 meV was selected. A polycrystalline sample (about 60 g) was filled in a hollow cylinder of 6 cm diameter and 12 cm height made from thin aluminium foil (the thickness of the sample was about 1-1.5 mm) and mounted in the sample chamber in transmission geometry. INS data were collected simultaneously by 12 detectors at constant scattering angles Θ in the range of $28^o<\Theta<134^o$. This covers the kinematical range $Q(E_0)$ from 1.4 to 4.4 Å^{-1} and energy transfers $\varepsilon=E-E_0$ between -7 (negative values correspond to neutron energy loss) and 120 meV (neutron energy gain). A vanadium sample was used for normalization runs, and the empty container was measured for each specific experimental condition. The energy resolution of the spectrometer (full width at half maximum of the elastic peak in the spectra taken with the vanadium sample) was about 5-8% for the measured energy transfers ($\Delta E \sim 1.3$ and 0.9 meV for the measurements on AgCuSe and AgCuS, respectively).

The essential data processing for the reduction of data from a time-of-flight inelastic neutron spectrometer are well described in [75]. Only a short overview of the data handling is therefore described here. Hence, the standard corrections for the background due to the empty container (taking into account the self-shielding of the sample), normalization and

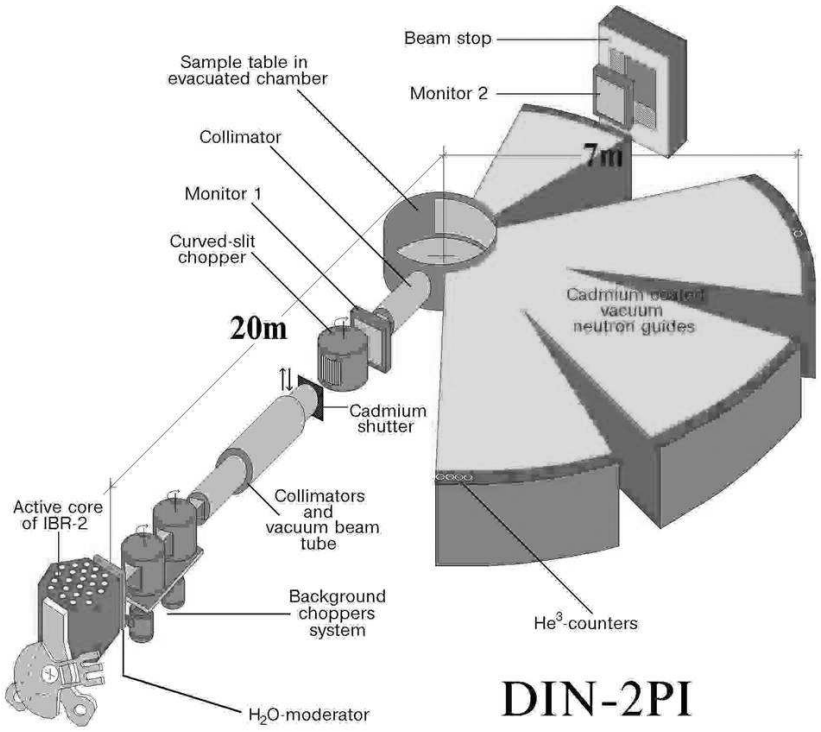

Figure 3.3: Schematic representation of the DIN-2PI direct geometry spectrometer installed at the IBR-II pulsed neutron reactor in Dubna, Russia

detector efficiency corrections were applied to correct the measured inelastic intensities in order to derive double differential scattering cross-sections $\frac{d^2\sigma}{d\Omega \cdot dE}$ for both samples by the standard data reduction procedure at DIN-2PI [76]. From the corrected double differential scattering cross-section the symmetrized dynamical structure factor (scattering law) $S(Q, \varepsilon)$ at constant scattering angle was calculated:

$$S(Q,\varepsilon) = \frac{4\pi}{\sigma_{sc}} \cdot (E_0/E)^{\frac{1}{2}} \cdot \frac{d^2\sigma}{d\Omega \cdot dE} \cdot e^{-\beta/2} \tag{3.1}$$

$$\beta = \varepsilon / k_B T \tag{3.2}$$

$e^{-\beta/2}$ is the symmetrization factor according to the detailed balance condition $S(Q,-\varepsilon) = e^{-\beta} \cdot S(Q,\varepsilon)$; σ_{sc} is the bound scattering cross-section of the scattering unit, $\hbar Q$ is the scattering angle- and energy-dependent modulus of the momentum transfer in the isotropic sample

$$\hbar Q = (2m[E_0 + E - 2(E_0 E)^{\frac{1}{2}} cos\Theta])^{\frac{1}{2}} \tag{3.3}$$

In these equations m is the mass of the neutron, k_B is the Boltzmann constant and T is the temperature at which the experiment was performed. No corrections were made for the

finite resolution of the spectrometer. Since the absorption cross sections of the samples at the selected incident energies were sufficiently large and a thin slab or hollow cylindrical sample holders were used, multiple scattering effects could be neglected [77].

The generalized frequency distribution was determined from the sum of the double differential scattering cross-section, weighted with the sine of the corresponding scattering angle. For incoherently scattering cubic crystals with Bravias lattices the measured one-phonon part of the double differential scattering cross-section at each momentum transfer is directly related to the phonon density of states. The main scattering from AgCuSe and AgCuS is coherent, nevertheless, an estimation of the generalized frequency spectrum is possible. In this case, according to the incoherent approximation [78], coherence effects should be of minor importance if a time-of-flight experiment is performed on a powder sample (directional averaging) with a sufficiently large incident energy (some meV) and in such a large kinematical range. Thus, we employed the incoherent approximation and used the following expression to obtain the frequency distribution $g(\varepsilon)$:

$$g(\varepsilon) = \frac{4\pi}{\sigma_{coh}} \sqrt{\frac{E_0}{E}} \varepsilon (1 - e^{-\beta}) \frac{8M\sqrt{E_0 E}}{N\hbar^2 (Q_{max}^4 - Q_{min}^4)} \int_{\Theta_{min}}^{\Theta_{max}} e^{2W(Q)} \left(\frac{d^2\sigma_{coh}}{d\Omega dE} \right) sin\Theta d\Theta \qquad (3.4)$$

where σ_{coh} is the bound coherent scattering cross-section and Q_{min} and Q_{max} are the smallest and largest momentum transfers, for which the intensity at the energy transfer ε was measured in the experiment. For polymorphic substances (as in this case) only a generalized frequency distribution $G(\varepsilon)$ can be derived. Each scattering element according to its concentration, cross-section, mass and Debye-Waller factor contributes to $G(\varepsilon)$. Hence, generalized frequency distributions $G(\varepsilon)$ of AgCuSe and AgCuS were derived from the presented experimental inelastic scattering data.

The multiphonon correction was performed according to the self-consistent iterative procedure well described in [75, 79, 80]. The total measured spectrum, $G(\varepsilon)$, is the sum of all components, $\sum_{n=0}^{\infty} G_n(\varepsilon)$, from neutrons scattered after creating different numbers, n, of phonons in the sample. Only the one-phonon scattering is useful for obtaining a phonon neutron-weighted density of states. So it is important to estimate the higher-order terms and subtract them, because multiphonon effects should be rather high at elevated temperatures and due to the very high amplitude of thermal motion in AgCuSe and AgCuS. Hence, a mul-

tiphonon expansion is done in two steps: first, the weights of the different n-components are calculated independently with input information on Q and atom displacements u at the temperature T; second, the spectral shape of each component $G_n(\varepsilon)$ is obtained by sequentially convoluting the one-phonon profile with itself $n-1$ times. Thereafter, multiphonon contributions were subtracted from the total measured spectrum, $G(\varepsilon)$, in an iterative way [75,79,80]. Finally, the frequency spectra below 1.5-2.5 meV were dominated by a large elastic peak due to resolution effects, nevertheless, this peak was easily fitted and removed, so that finally data below 1.5-2.5 meV were extrapolated to zero transferred energy in a Debye-like form.

Chapter 4

Preliminary characterization of the samples

Preliminary X-ray diffraction measurements at RT (see figure 4.1) confirm the superionic β-phase for $Cu_{1.75}Se$, non-superionic α-phase for Cu_2Se, whereas $Cu_{1.85}Se$ consists of a mixture of α-Cu_2Se (PDF-2 card [27-1131]) and β-$Cu_{1.8}Se$ (PDF-2 card [71-44]) in a ratio corresponding to a stoichiometry of 1.85. The results of X-ray diffraction measurements are in agreement with the phase diagram published in [16, 27].

STA measurements on $Cu_{1.75}Se$ and $Cu_{1.85}Se$ are shown in figure 4.2. The results look similar for both samples: DSC-curves do not show thermal effects up to 650 K; several consecutive thermal effects observed above 650 K are most probably connected with the formation of copper and selenium oxides. These effects correlate to a strong increase of the samples weight observed in TG-curves at this temperature. Note that the $\beta + \alpha \longrightarrow \beta$ phase transition in $Cu_{1.85}Se$ is not detected in a DSC experiment, however, a pure β-phase was observed in the diffraction pattern of $Cu_{1.85}Se$ at 353 K. On the other hand, STA measurements were performed in inert atmosphere on $Cu_{2-\delta}Se$ and are illustrated in figure 4.3. A strong decrease of the samples weight can be observed in the TG curve above 800 and 600 K for Cu_2Se and $Cu_{1.75}Se$, respectively. This effect is more probably due to the evaporation of selenium from the samples. Some strong endothermic signals in the DSC curves occur after this temperature, where a pronounced evaporation of selenium is proposed. They can be associated with an ongoing decomposition of the samples at high temperatures

or with reactions of the samples with the sample holder. After such a reaction no useful information about the investigated material can be obtained. Thus, in order to allow a direct comparison of our results with literature data, high-temperature synchrotron diffraction measurements were performed on these compounds in air, to determine the corresponding stability ranges and to take this important experimental information on the thresholds for decomposition into account.

A qualitative overview of the changes in the diffraction patterns of Cu_2Se with increasing temperature is shown in figure 4.4. At 423 K the diffraction patterns of Cu_2Se correspond to the superionic β-phase (PDF-2 card [79-1841]). The superionic phase transition in Cu_2Se was also observed in the DSC-curve at 414 K (see figures 4.2 and 4.3). This is in good agreement with other references (see table 2.2). Simultaneously with the phase transition a release of copper occurs [29] which already starts before the phase transition. A slight increase of the sample weight of Cu_2Se has been observed by TG measurements at temperatures higher than 450 K (see figure 4.2). This is connected to an oxidation of the free copper. Oxidation of copper during heating is not yet fully understood [81, 82]. The process of copper release from Cu_2Se and the oxidation of free copper can be analyzed on the basis of STA results and the temperature dependence of the lattice parameter in β-Cu_2Se, shown in figure 4.4.

Diffraction measurements reveal a decrease of the lattice parameter in Cu_2Se during heating in the temperature range between 423 - 543 K under two competitive processes: thermal lattice expansion and decrease of copper content. In the consecutive temperature range 543 - 573 K the lattice parameter increases linearly. According to our results copper release is completed at about 543 K when the initial composition Cu_2Se has changed to $Cu_{1.95}Se$ and does not change any more up to 573 K. The composition of $Cu_{1.95}Se$ in this temperature range was deduced from a comparison with measured lattice parameters $a(T, \delta)$ of $Cu_{2-\delta}Se$ [16]. At 583 K a sudden change in the temperature dependence of the lattice parameter occurs, which correlates with a peak in the DSC curve at 600 K and an anomaly in the slope of the TG curve (mark 2 in figure 4.2). The peak in the DSC curve is most probably connected to a formation of Cu_2O; the first traces of Cu_2O appear in the diffraction patterns above 600 K (see figure 4.4). According to [81] CuO and Cu_2O are formed during heating of bulk copper in dry air at 458 and 650 K, respectively. At temperatures above 650

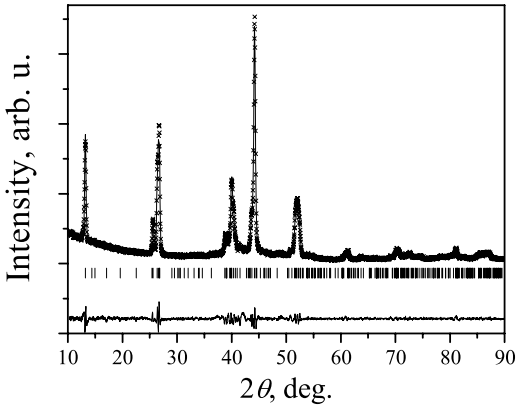

(a) α-Cu_2Se at RT (CuKα_1)

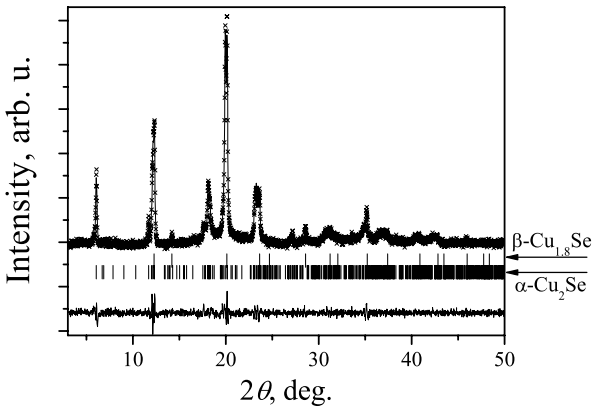

(b) $Cu_{1.85}Se$ (α-Cu_2Se + β-$Cu_{1.8}Se$) at RT (MoKα_1)

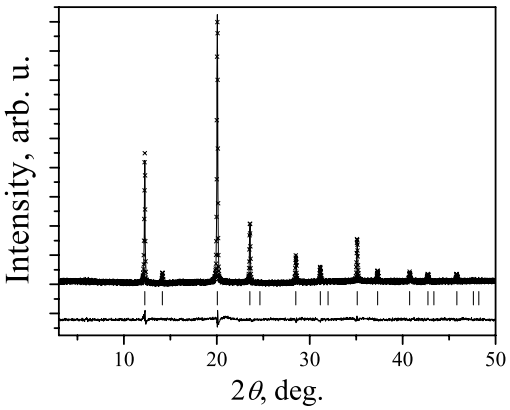

(c) β-$Cu_{1.75}Se$ at RT (MoKα_1)

Figure 4.1: X-ray diffraction patterns of $Cu_{2-\delta}Se$ samples: (a), (b) – structurally independent (Le Bail) fits to the data according to references [35, 57]; (c) – result of a Rietveld refinement according to references [36,57]. Crosses are experimental data, the line represents the calculated profile and the curve at the bottom is their difference. The vertical lines show the calculated positions of the Bragg peaks.

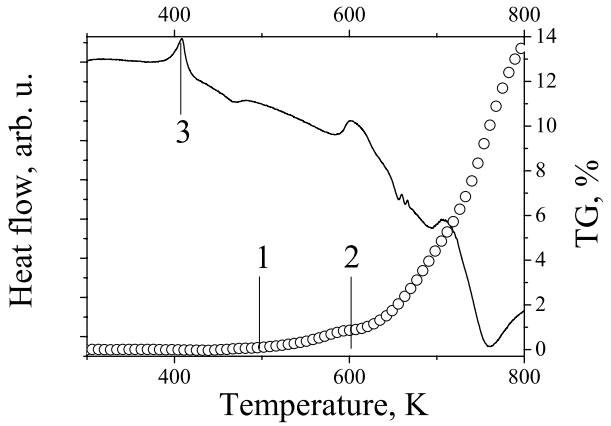

(a) Cu_2Se (10 K/min)

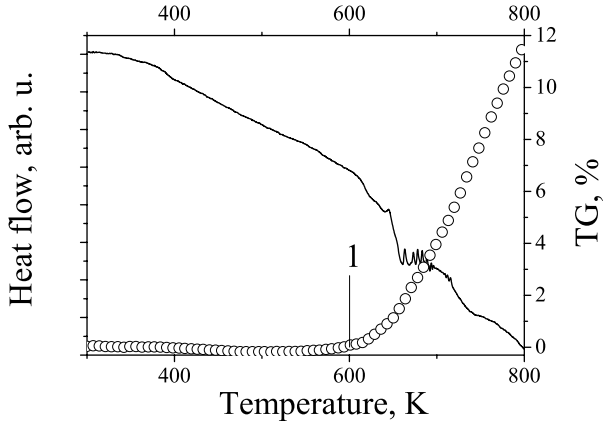

(b) $Cu_{1.85}Se$ (10 K/min)

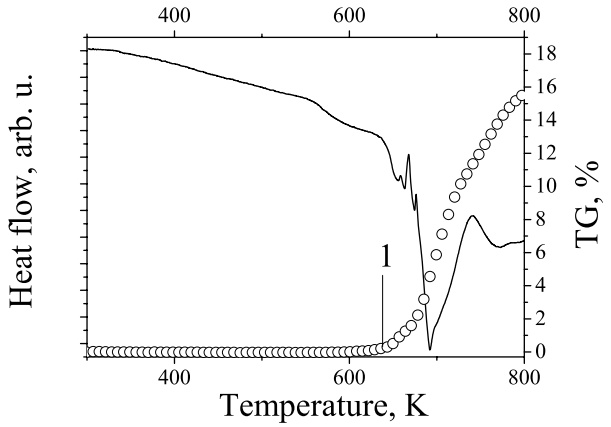

(c) $Cu_{1.75}Se$ (10 K/min)

Figure 4.2: STA results for $Cu_{2-\delta}Se$ samples measured in air. Solid lines and open circles correspond to DSC and TG curves, respectively. 1 and 2 mark changes of the slope in the TG curves; 3 marks the temperature of the superionic $\alpha \longrightarrow \beta$ phase transition.

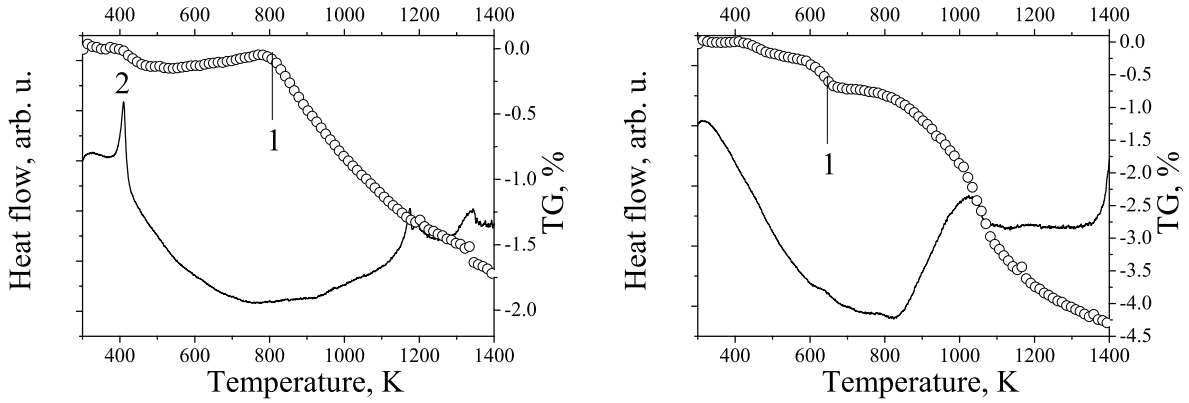

(a) Cu_2Se (10 K/min) (b) $Cu_{1.75}Se$ (10 K/min)

Figure 4.3: STA results in inert argon atmosphere for Cu_2Se and $Cu_{1.75}Se$. Solid lines and open circles correspond to DSC and TG curves, respectively. 1 – temperature threshold for strong selenium evaporation from the sample; 2 – the temperature of the superionic $\alpha \longrightarrow \beta$ phase transition.

K both copper oxides, Cu_2O and CuO, form a binary film on the surface of bulk copper. At higher temperatures CuO gradually disappears whereas more and more Cu_2O is formed [81]. Noted that no diffraction peaks of Cu and CuO have been observed between RT and 573 K. Above 600 K the slope in the TG curve becomes steeper; the DSC curve displays several consecutive thermal effects, which can be related to the formation of oxides of selenium and copper. X-ray diffraction performed on $Cu_{2-\delta}Se$ ($\delta = 0, 0.15, 0.25$) samples at RT after STA measurements up to 823 K in air, indicate a decomposition to copper oxide CuO (PDF-2 card [45-937]) and copper oxide selenite $Cu_2O(SeO_3)$ (PDF-2 card [46-793]).

Because of the instability of Cu_2Se, the structure of Cu_2Se has only been analyzed in the ranges 423 - 473 K and 553-573 K (with composition $Cu_{1.95}Se$). Due to the oxidation of the samples the maximum temperature in the diffraction measurements on $Cu_{1.75}Se$, $Cu_{1.85}Se$ and $Cu_{1.95}Se$ was restricted to 573 K. To verify the phase composition of our samples after synchrotron measurements, diffraction patterns for all compounds were collected after heating again at the lowest initial experimental temperatures.

Preliminary conventional X-ray diffraction measurements on Ag_3CuS_2 (figure 4.5) revealed some additional reflections from $Ag_{1.2}Cu_{0.8}S$ (PDF-2 card [12-152]) in the sample. Nevertheless, these impurity traces were very weak and neglected. No STA measurements were performed for this sample. All high-temperature diffraction measurements were made under argon atmosphere. The analysis of the diffraction pattern from the sample after heat

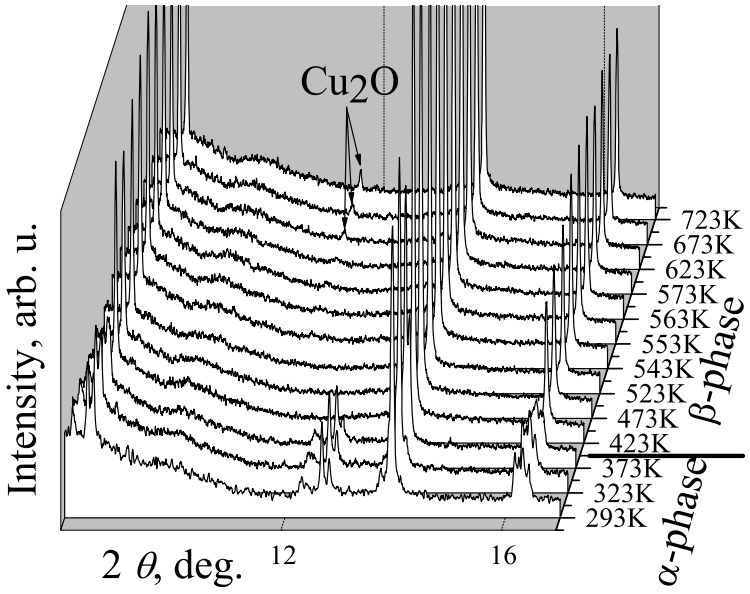

(a)

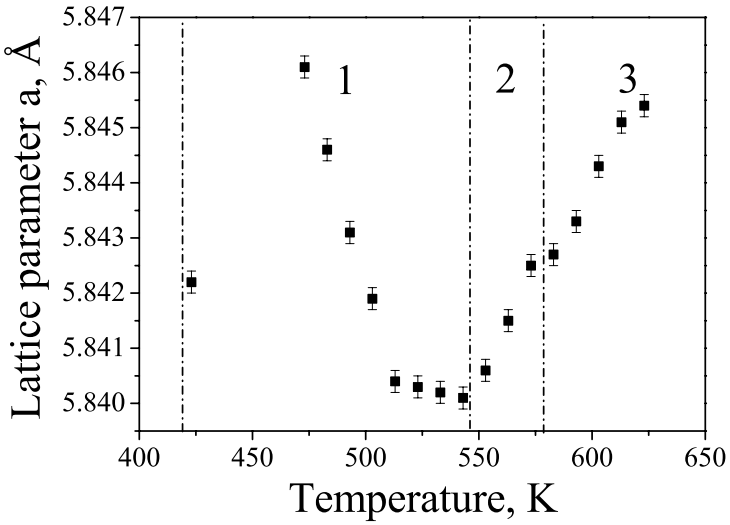

(b)

Figure 4.4: (a) – low angle region of selected synchrotron powder diffraction patterns (λ=0.50970 Å) from Cu_2Se; the changes in diffraction patterns at the superionic $\alpha \longrightarrow \beta$ phase transition and the appearance of a weak diffraction line from Cu_2O can clearly be seen. (b) – the temperature dependence of the lattice parameter in β-Cu_2Se sample during heating; the following temperature ranges are marked in the figure: 1 - change of lattice parameter under two competitive processes: thermal lattice expansion and decrease of the copper content; 2 - thermal expansion of β-$Cu_{1.95}Se$; 3 - thermal expansion and ongoing oxidation of the sample.

treatment in argon showed no changes with respect to the initial state, *i. e.*, the sample was stable in argon at high-temperatures.

After preliminary X-ray diffraction measurements, which revealed no impurities in the sample, AgCuSe was characterized by STA (figure 4.6). The DSC curve of AgCuSe measured in air displays a strong endothermic signal at 480 K, which corresponds to the superionic phase transition. This is in agreement with calorimetric, X-ray diffraction measurements and ionic conductivity data from the literature [12, 13, 42, 45, 47, 49]. The TG curve clearly indicates an increase of the sample weight during heating in air. This corresponds to an oxidation of the sample. X-ray diffraction phase analysis showed decomposition of the initial sample into copper oxide (PDF-2 card [45-937]), silver selenite (PDF-2 card 34-382) and silver (PDF-2 card [89-3722]). A possible oxidation mechanism of AgCuSe is suggested in [83]. On the other hand, no obvious changes of the sample weight were observed in the TG curve measured in argon (see figure 4.6). X-ray diffraction analysis of the sample, which was heated in argon during STA, showed no significant changes with respect to the initial state. The DSC heating curve of AgCuSe in argon exhibits two pronounced endothermic peaks with maxima at 480 and 1054 K, corresponding to the superionic phase transition and the melting of the sample, respectively. The DSC data during successive cooling show thermal events at 464 and 1042 K, *i.e.* a minor hysteresis in comparison with heating.

Preliminary conventional X-ray diffraction measurements revealed no impurities in AgCuS, afterwards this sample was characterized by STA (figure 4.7). The DSC curve of AgCuS measured in air displays a strong endothermic signal at ∼370 K, which corresponds to the orthorhombic ⟶ hexagonal phase transition. This is in agreement with our diffraction studies and with data from [51, 54, 55]. An additional weak endothermic effect with a maximum at about ∼405 K could be associated with the low-temperature boundary of the two-phase hexagonal-cubic region corresponding well with our (about ∼399 K) and Skinners's (400.5 K) [55] value from diffraction measurements. During heating in air the TG curve clearly indicates a change of the sample weight above ∼535 K, which is related to a decomposition of the sample and reactions with the sample holder. Therefore, no X-ray diffraction pattern of the sample after the STA measurements in air was taken. On the other hand, no obvious changes of the sample weight were observed in the TG curve measured

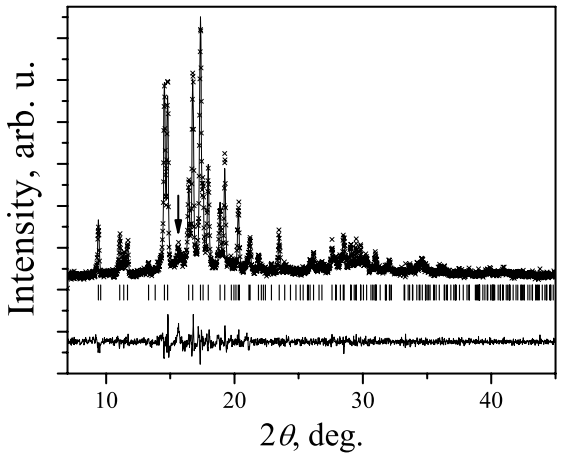

Figure 4.5: The X-ray diffraction pattern of Ag_3CuS_2 (MoKα_1). The result of the Rietveld refinement according to reference [56] is illustrated. A weak reflection from $Ag_{1.2}Cu_{0.8}S$ is marked by pointer.

under argon. X-ray diffraction analysis of the sample after heat treatment in argon showed no changes with respect to the initial state. The DSC heating curve of AgCuS in argon exhibits in addition a strong endothermic signal with its maximum at ∼936 K indicating the melting of the sample.

Thus, STA and diffraction measurements revealed that the samples AgCuSe, AgCuS and Ag_3CuS_2 are stable in inert argon atmosphere even at high temperatures, in contrast to $Cu_{2-\delta}Se$.

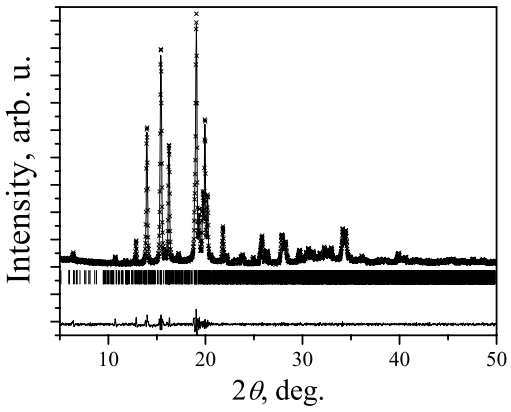

(a) β-AgCuSe at RT (MoKα_1)

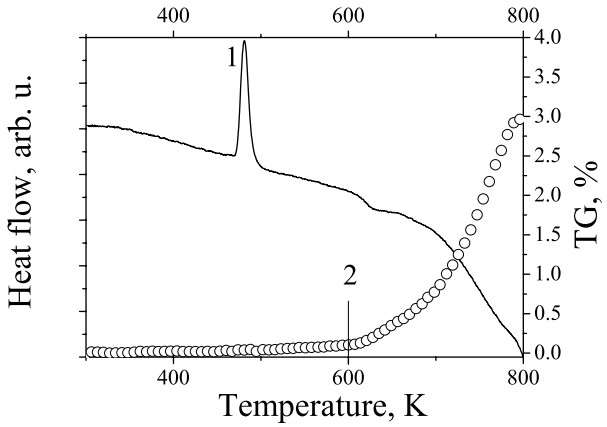

(b) AgCuSe in air (10 K/min)

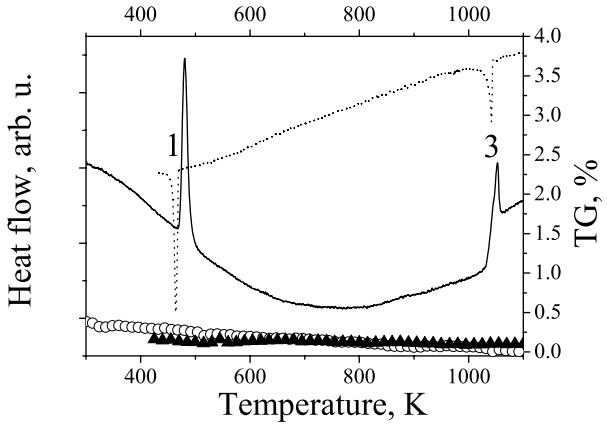

(c) AgCuSe in argon (10 K/min)

Figure 4.6: Plot (a) shows the result of structurally independent (Le Bail) fit for β-AgCuSe according to reference [47]. Plots (b) and (c) represent STA traces for AgCuSe. Solid and dotted lines in plots (b) and (c) are DSC curves recorded during heating and cooling, open and closed symbols are TG curves at heating and cooling, respectively; 1 - peak which corresponds to the superionic phase transition; 2 - temperature threshold for decomposition; 3 - peak which corresponds to the melting point.

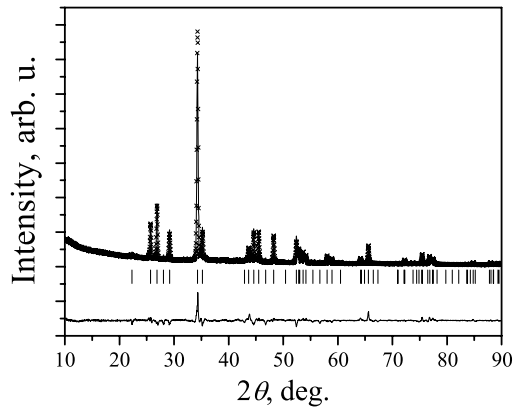

(a) β-AgCuS at RT (CuKα_1)

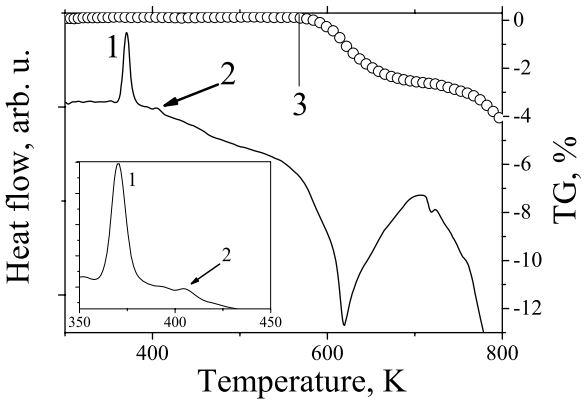

(b) AgCuS in air (10 K/min)

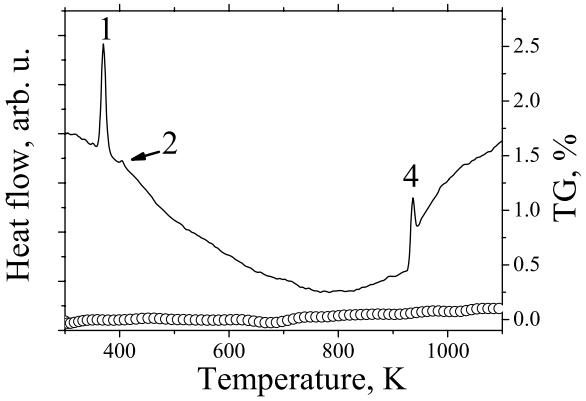

(c) AgCuS in argon (10 K/min)

Figure 4.7: The result of a Rietveld refinement according to [50] and STA traces for AgCuS. Solid lines and open symbols in plots (b) and (c) are DSC and TG curves recorded during heating; 1, 2 - peaks which correspond to the superionic phase transitions; 3 - temperature threshold for decomposition; 4 - peak which corresponds to the melting point.

Chapter 5

Diffraction results and their discussion

5.1 High-temperature synchrotron powder diffraction on berzelianite, $Cu_{2-\delta}Se$ (δ=0, 0.15, 0.25)

5.1.1 Phase transitions and thermal expansion of β-$Cu_{2-\delta}Se$

The unit cell parameters of β-$Cu_{2-\delta}Se$ with δ = 0.05, 0.15, 0.25 as a function of temperature are shown in figure 5.1, determined from powder synchrotron diffraction. The temperature dependencies of lattice parameters for $Cu_{1.75}Se$, $Cu_{1.85}Se$ and $Cu_{1.95}Se$ were fitted by linear functions, and thermal expansion coefficients of $26.6 \cdot 10^{-6} K^{-1}$, $23.8 \cdot 10^{-6} K^{-1}$ and $16.3 \cdot 10^{-6} K^{-1}$ were derived respectively. The decrease of the thermal expansion coefficient with a decrease of δ should be noted; this confirms previous results [16, 27].

Examples of experimental and calculated diffraction patterns for β-$Cu_{2-\delta}Se$ are shown in figure 5.2. The continuous decrease of the (200) Bragg reflection at higher temperatures is clearly observed in the diffraction patterns of β-$Cu_{1.75}Se$ and β-$Cu_{1.85}Se$ (see figure 5.3). This phenomenon might be an evidence of a diffuse phase transition, which occurs between 350 - 523 K for $Cu_{1.75}Se$ and 473 - 533 K for $Cu_{1.85}Se$. Recently, temperature induced changes of the intensity of the 111 reflection were associated with a similar diffuse phase transition in fcc Li_2S around 900 K [84]. A variation of the reflection intensity can be attributed to the existence of the low- and high-temperature structure modifications characterized by a redistribution and absence of redistribution of copper ions with temperature [21, 27]. Since no accurate

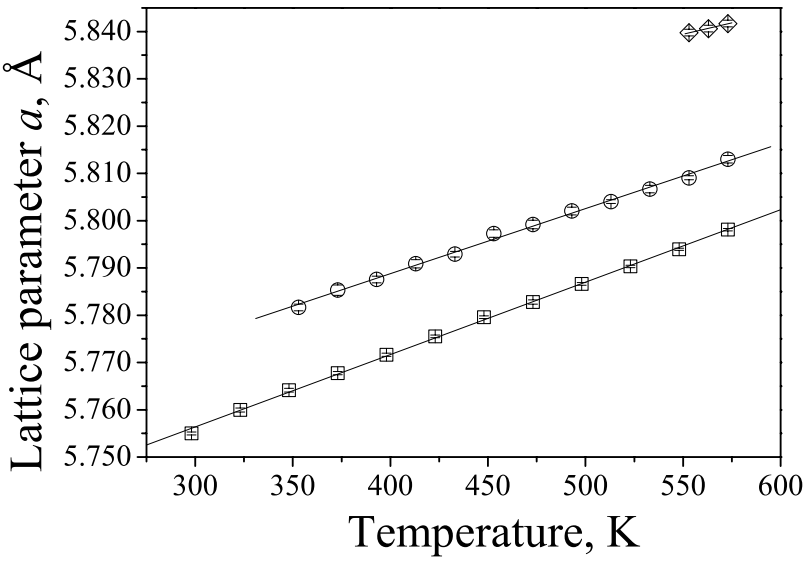

Figure 5.1: The unit cell parameter of β-$Cu_{2-\delta}Se$ with δ values of 0.05 (diamonds), 0.15 (circles) and 0.25 (squares) as a function of temperature determined from synchrotron powder diffraction. The lines correspond to approximated functions fitted to experimental points as it is described in the text.

analysis of the distribution of copper ions in the samples with different stoichiometries has been reported so far, such an analysis will be presented in the next subsection.

5.1.2 Structural behaviour of superionic β-$Cu_{2-\delta}Se$

The copper ion distribution has been analyzed by different structural models in which the fcc lattice array is formed by selenium atoms and copper cations are distributed over different interstitial sites with overall symmetry $Fm\bar{3}m$. Great care was taken to ensure that data have not been overinterpreted by models with an inappropriately large number of structural parameters. This analysis allows to establish differences in the time and spatial averaged distribution of copper for different stoichiometric compositions of copper selenide β-$Cu_{2-\delta}Se$ and its temperature dependence. We used the so called "split-site" approach (see [2] for details) to introduce a disorder in β-$Cu_{2-\delta}Se$. For instance, in the frame of the split-site model each of the 8(c) and 4(b) sites (space group $Fm\bar{3}m$) can be splitted into four 32(f) sites at (x, x, x) with $\frac{1}{4}<x<\frac{1}{3}$ and 32(f) at (x, x, x) with $\frac{1}{3}<x<\frac{1}{2}$. Occupation of the 32(f) positions results in $\langle 111 \rangle$ as the preferred direction for the ionic motion, whereas a

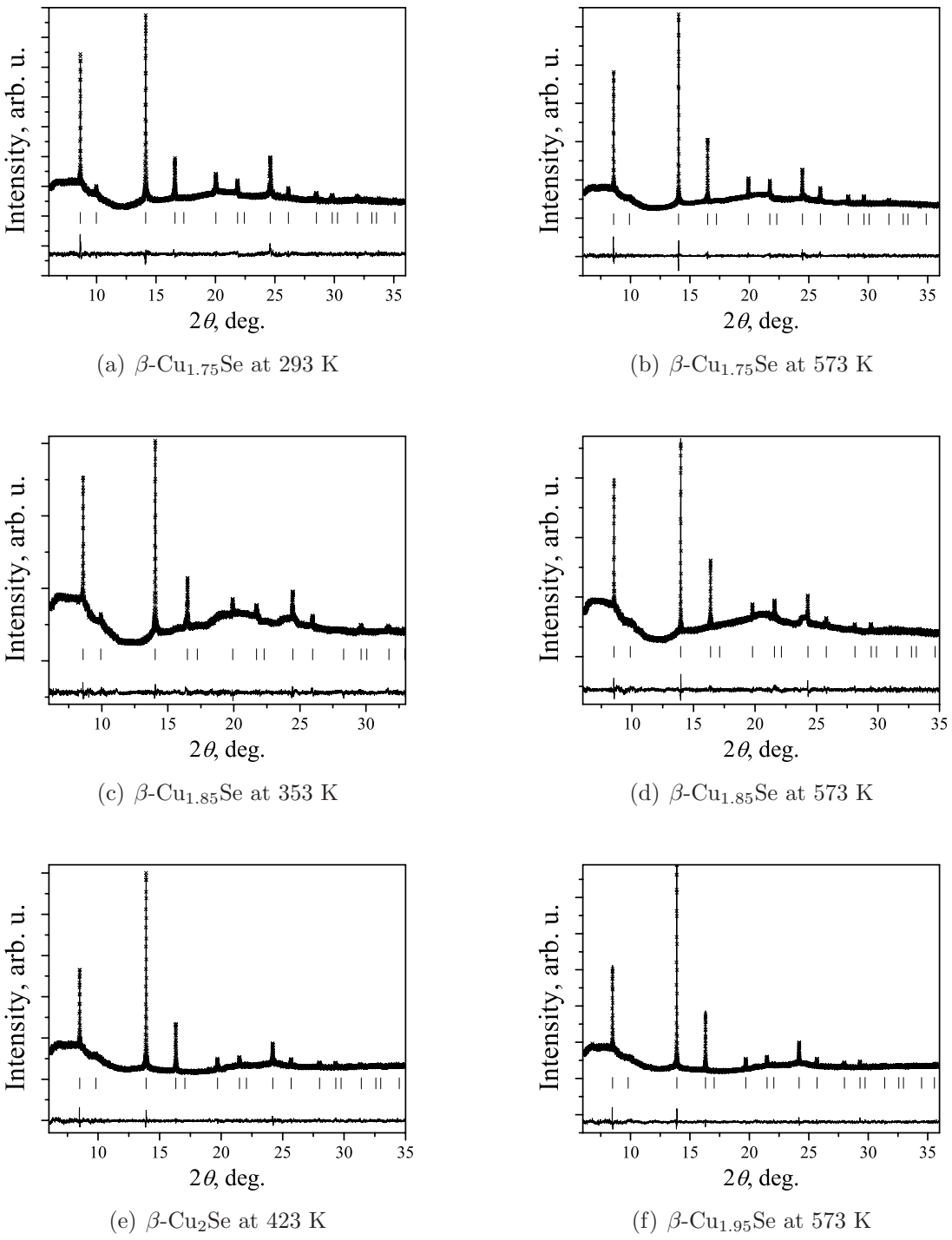

(a) β-$Cu_{1.75}Se$ at 293 K

(b) β-$Cu_{1.75}Se$ at 573 K

(c) β-$Cu_{1.85}Se$ at 353 K

(d) β-$Cu_{1.85}Se$ at 573 K

(e) β-Cu_2Se at 423 K

(f) β-$Cu_{1.95}Se$ at 573 K

Figure 5.2: Synchrotron powder diffraction patterns of β-$Cu_{2-\delta}Se$ (λ = 0.49993 Å). The Rietveld fits were based on the model with cations on tetrahedral 8(c) and octahedral 32(f) sites. Crosses are experimental data, the lines are calculated profiles and the lower curves their differences. Tick marks show the calculated positions of β-$Cu_{2-\delta}Se$ reflections.

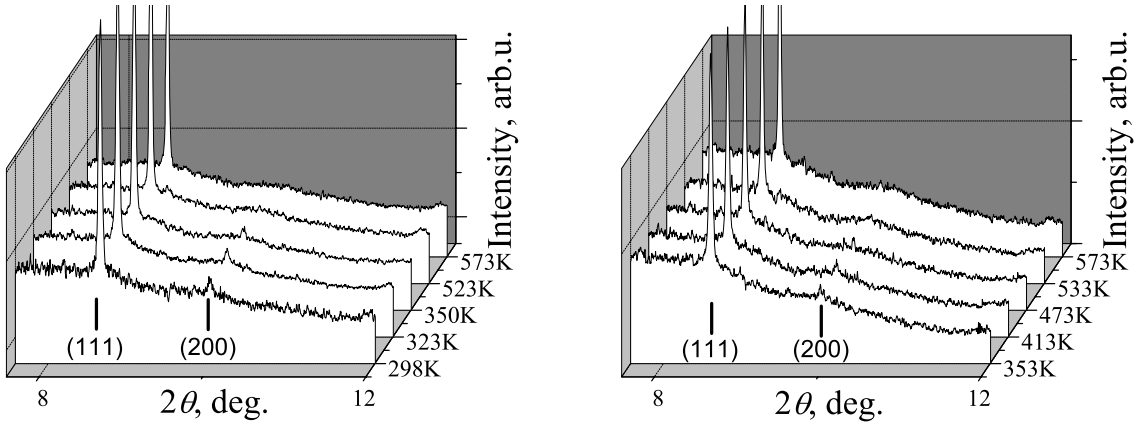

(a) β-$Cu_{1.75}Se$ (b) β-$Cu_{1.85}Se$

Figure 5.3: Sections of the synchrotron powder diffraction patterns showing the thermal evolution of the (200) reflection ($\lambda = 0.49993$ Å).

distribution of ions over 48(g) sites at (x, $\frac{1}{4}$, $\frac{1}{4}$) results in $\langle 100 \rangle$ as the preferred direction of motion.

Table 5.1 shows a number of models for the disordered structures of the cations in $Cu_{1.75}Se$, derived from data collected with a NaI scintillation counter (*i. e.* in a high-resolution and low-background mode). Model 1 is the ideal anti-fluorite structure formed by the selenium sublattice with copper cations located at the ideal tetrahedral interstices on the 8(c) site. Model 1 can be considered as a starting point, which gave rather good refinement results for all samples. An improved agreement in the refinement was obtained by including the occupation on the copper sites as model parameters. A lower copper content than estimated from initial stoichiometry was refined. This is a clear indication of disorder but does not provide reliable information about the actual positions. Model 2 mimics the effect of anharmonicity on the tetrahedral site by splitting the 8(c) ($\frac{1}{4}$, $\frac{1}{4}$, $\frac{1}{4}$) cation site into 32(f) (x, x, x) sites. Instead of one single copper cation located in the center of the tetrahedron, the cation is distributed over a set of four symmetry equivalent sites, which are shifted off the center of the tetrahedra in $\langle 111 \rangle$ direction. In the refinement process the x value of the 32(f) site and the isotropic thermal displacement factors for copper and selenium ions were refined. The total content of copper ions in the unit cell was fixed according to the initial stoichiometry. This model gives a better fit with respect to the agreement factor than model 1. Model 3 contains an additional possible site for the copper ions on the

ideal octahedral 4(b) site. This model improves the agreement, but the isotropic thermal displacement parameter for the copper ions in the octahedral sites became very large, if no constraint between thermal parameters of copper in different split sites was applied. Model 4 includes two possible positions for the copper ions: the ideal tetrahedral 8(c) site and the 32(f) site ($\frac{1}{3}<x<\frac{1}{2}$), where the copper ions are distributed between sites away from ($\frac{1}{2}$, $\frac{1}{2}$, $\frac{1}{2}$) in $\langle 111 \rangle$ directions within the octahedral voids. In model 5 the 8(c) and 4(b) sites were split simultaneously into two different 32(f) sites. In analogy to models 1-4 the total content of copper ions in the unit cell was fixed in the refinement. However, the correlation between the refined parameters was too high for a reliable independent determination. Further attempts were made to refine a model with a splitting of the 8(c) into a 48(g) site (x, $\frac{1}{4}$, $\frac{1}{4}$) (Cu ion disordering in $\langle 100 \rangle$ directions) or with anisotropic temperature factors in some of the previously described models. However, all these models gave a very high correlation between the parameters and a numerical instability in the refinement process. Model 4 (see figure 5.4) is therefore the preferred average structure model for β-$Cu_{1.75}Se$, not only because of the slightly better fit, but also because of the more realistic copper thermal displacement parameter and the more convincing disorder in the direction to the faces of the octahedra, rather than to the octahedra edges. Data for $Cu_{1.85}Se$ and $Cu_{1.95}Se$ were collected using the image plate detector. For data analyses the average structural model for β-$Cu_{1.75}Se$, derived from high-resolution and low-background data, was used.

The results of the modelling can be summarized as follows: copper ions are distributed predominantly over the tetrahedrally coordinated sites with a significant cation density on the octahedral interstices. In addition the occupancy of the 32(f) sites indicates that copper ions within the tetrahedral cavities undergo extensive anharmonic thermal vibrations in the $\langle 111 \rangle$ directions and will, on occasion, turn into a neighbouring octahedron. However, the cation does not undergo diffusion in this direction through the center of the octahedron, which is the 4(b) ($\frac{1}{2}$, $\frac{1}{2}$, $\frac{1}{2}$) position. A considerable decrease of the R-Bragg factor by splitting of the 4(b) site into a 32(f) site and a huge thermal displacement factor for copper ions on the 4(b) site shows that the cation density has a minimum on the ideal octahedral site 4(b). Octahedral sites are, therefore, considered as positions with a lower probability density. Therefore, a cation diffusion mechanism with cation jumps between nearest neighbour sites

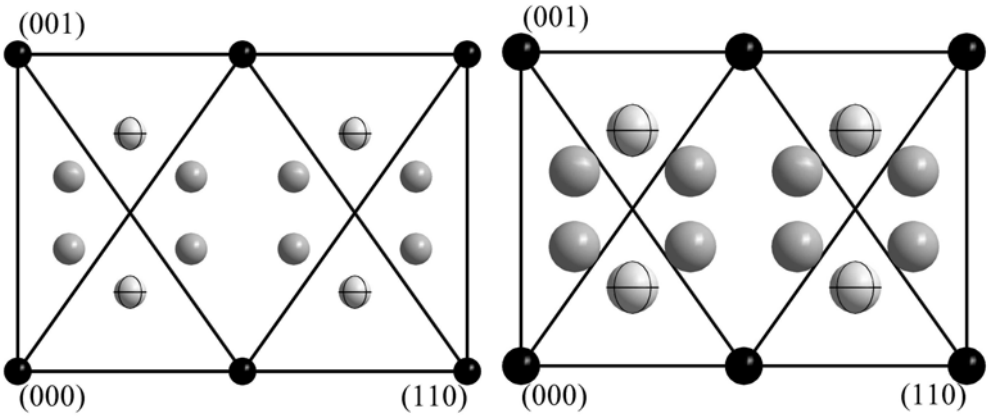

(a) β-$Cu_{1.75}Se$ at RT (b) β-$Cu_{1.75}Se$ at 573 K

Figure 5.4: Schematic representation of the average structure of superionic β-$Cu_{1.75}Se$ according to model 4 from table 5.1. The plots show a (110) section through the unit cell with 100% occupancy for all crystallographic sites. The diagonal lines indicate the positions of the boundaries between tetrahedral and octahedral interstices. Black spheres, grey spheres with inner lines and grey spheres are Se^{2-} on the 4(a), Cu^{+} on the ideal tetrahedral 8(c) and Cu^{+} on the octahedral 32(f) sites, respectively.

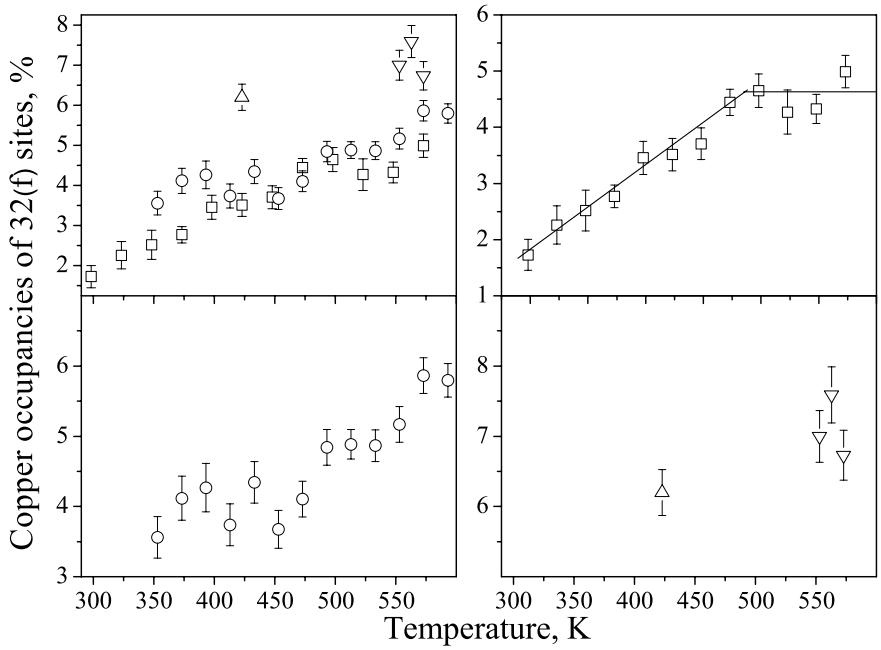

Figure 5.5: Copper site occupancies on 32(f) at (x, x, x) with $\frac{1}{3} < x < \frac{1}{2}$ in β-$Cu_{1.75}Se$ (squares), β-$Cu_{1.85}Se$ (circles), β-$Cu_{1.95}Se$ (inverse triangles) and β-Cu_2Se (triangle).

Table 5.1: Structural models of β-$Cu_{1.75}Se$ at lowest and highest experimental temperatures. Refined structural parameters: isotropic thermal displacements, copper positional parameters and copper site occupancies; copper isotropic thermal parameters and occupancies were constrained during refinements.

$Fm\bar{3}m$, Z=4, T=298 K, a=5.7550(2) Å					
Model, №	1	2	3	4	5
Se, site	4(a) at (0,0,0)				
u_{iso} (Å^2)	0.015(1)	0.014(1)	0.018(1)	0.024(2)	0.029(2)
Occupancy (%)	100	100	100	100	100
Cu, site	8(c)	32(f)	8(c)	8(c)	32(f)
x	$\frac{1}{4}$	0.278(2)	$\frac{1}{4}$	$\frac{1}{4}$	0.230(3)
y	$\frac{1}{4}$	0.278(2)	$\frac{1}{4}$	$\frac{1}{4}$	0.230(3)
z	$\frac{1}{4}$	0.278(2)	$\frac{1}{4}$	$\frac{1}{4}$	0.230(3)
u_{iso} (Å^2)	0.046(1)	0.018(5)	0.043(1)	0.030(2)	0.001(7)
Occupancy (%)	87.5	21.875	85.9(5)	80.7(3)	19.7(3)
Cu, site	–	–	4(b)	32(f)	32(f)
x	–	–	$\frac{1}{2}$	0.386(6)	0.377(4)
y	–	–	$\frac{1}{2}$	0.386(6)	0.377(4)
z	–	–	$\frac{1}{2}$	0.386(6)	0.377(4)
u_{iso} (Å^2)	–	–	0.043(1)	0.030(2)	0.001(7)
Occupancy (%)	–	–	3.20(10)	1.7(3)	2.2(3)
R_B	0.0469	0.0330	0.0372	0.0188	0.0187
R_F	0.0353	0.0261	0.0373	0.0141	0.0158
χ^2	1.55	1.5	1.48	1.51	1.41
$Fm\bar{3}m$, Z=4, T=573 K, a=5.7981(1) Å					
Model, №	1	2	3	4	5
Se, site	4(a) at (0,0,0)				
u_{iso} (Å^2)	0.020(2)	0.018(1)	0.030(1)	0.048(2)	0.048(4)
Occupancy (%)	100	100	100	100	100
Cu, site	8(c)	32(f)	8(c)	8(c)	32(f)
x	$\frac{1}{4}$	0.296(1)	$\frac{1}{4}$	$\frac{1}{4}$	0.25(6)
y	$\frac{1}{4}$	0.296(1)	$\frac{1}{4}$	$\frac{1}{4}$	0.25(6)
z	$\frac{1}{4}$	0.296(1)	$\frac{1}{4}$	$\frac{1}{4}$	0.25(6)
u_{iso} (Å^2)	0.110(4)	0.033(4)	0.114(4)	0.067(4)	0.06(1)
Occupancy (%)	87.5	21.875	82(1)	67.50(10)	16.9(6)
Cu, site	–	–	4(b)	32(f)	32(f)
x	–	–	$\frac{1}{2}$	0.375(3)	0.375(4)
y	–	–	$\frac{1}{2}$	0.375(3)	0.375(4)
z	–	–	$\frac{1}{2}$	0.375(3)	0.375(4)
u_{iso} (Å^2)	–	–	0.114(4)	0.067(4)	0.06(1)
Occupancy (%)	–	–	9(3)	5.0(3)	5.0(6)
R_B	0.0727	0.0501	0.0593	0.0202	0.0209
R_F	0.0355	0.0321	0.0547	0.0260	0.0264
χ^2	1.79	1.57	1.64	1.35	1.35

via the periphery of the octahedral interstitials is proposed. The diffusion pathway does not exactly correspond to ⟨111⟩ or ⟨100⟩; it can be described as a "skewed" ⟨100⟩ direction rather than a ⟨111⟩ direction. The temperature dependence of the structure parameters in the frame of model 4 can be described as follows. The isotropic thermal displacement parameters of cations and anions increase monotonically with temperature in all compounds; the copper positional parameter x is temperature independent within estimated standard deviations. The copper population on the 32(f) site increases with copper content. The population on the 32(f) site increases with temperature. The simultaneous decrease of the 8(c) site occupation is due to the applied constraints in the refinement. The redistribution of copper ions between the 32(f) and 8(c) site with temperature is more pronounced in $Cu_{1.75}Se$ than in $Cu_{1.85}Se$ and $Cu_{1.95}Se$ as displayed in figure 5.5. The temperature dependence of the copper population on the 32(f) site in $Cu_{1.75}Se$ is characterized by two regions with different rates of increase of the site occupancy; the change of slope takes place at 470 K that correlates with the temperature of disappearance of the 200 Bragg reflection (*i.e.* with the onset of the diffuse phase transition).

Despite of the simplicity of our model and the absence of analysis of anisotropic terms, the results give additional indications of a thermally activated diffusion in β-$Cu_{2-\delta}Se$ with δ=0, 0.15, 0.25. In the frame of the split-site model static disorder and anharmonicity of the thermal vibrations of mobile ions are modelled by a splitting of the ideal tetrahedral and octahedral sites into partially occupied sites. X-ray diffraction can not distinguish these two effects (anharmonicity and static disorder). Nevertheless, our results show a diffusion pathway in β-$Cu_{2-\delta}Se$ through the periphery of the octahedral cavities. The occupancy on the 32(f) site should be a limiting factor for the copper ion diffusion, *i.e.*, the ionic conductivity in $Cu_{1.75}Se$ should be lower than in Cu_2Se and $Cu_{1.85}Se$ due to a lower occupation of the 32(f) site. This correlates well with the ionic conductivity measurements [10, 11], which have shown that ionic conductivity in $Cu_{2-\delta}Se$ decreases with an increase of δ. A diffusion process, limited by available vacancies, would result in the opposite effect.

Additional, diffraction investigations on β-$Cu_{2-\delta}Se$ in broader ranges of temperatures and compositions combined with ionic conductivity measurements might further elucidate the correlation of underlying structure and resulting conductivity in this system. In the light

of complications with such experiments due to decomposition of the samples at high temperatures, even in inert atmosphere, and the consistent interpretation of all experimental data in the derived model, the focus of the following work should be addressed to microstructural and dynamic aspects.

5.1.3 Microstructure features of β-$Cu_{1.75}Se$

Peak broadening in X-ray or neutron powder diffraction can be attributed to one or more of the following sources: instrumental broadening, finite crystallite size, the presence of micro-strain and/or extended defects (stacking faults, micro-twinning, dislocations, *etc.*) [71, 85]. An analysis of this effect with respect to the dependence of profile shape and half width on the diffraction angle can give important information about microstructure and morphology of a sample.

Peak broadening in the diffraction patterns of $Cu_{2-\delta}Se$ was mentioned for the first time [27]. Internal stress introduced during grinding of the samples in a mortar was suggested as the main reason for diffraction peak broadening. However, no analysis of peak broadening was reported. Therefore, a systematic analysis of the peak broadening in β-$Cu_{1.75}Se$ is reported here as a representative example for $Cu_{2-\delta}Se$.

The powder diffraction experiments on annealed and non-annealed β-$Cu_{1.75}Se$ samples were performed at beam-line B2 using a high-resolution and low-background NaI scintillation counter equipped with Ge (111) analyzer crystal in front. The seven most intensive diffraction maxima of annealed and non-annealed $Cu_{1.75}Se$ were measured at RT. Six reflections of the reference material LaB_6 (NIST SRM 660a) were measured with the same experimental setup and used to evaluate the resolution function of the diffractometer. Positions (2θ), full-width-at-half-maximum (FWHM) and the shapes of all reflections were analyzed individually using cmpr program [73]. Line profiles were modelled by a pseudo-Voigt function in symmetric approach. The integral breadth method based on a Williamson-Hall plot (see for example [72]) was applied for an estimation of the microstructure parameters.

Profiles of all measured reflections of LaB_6, annealed and non-annealed $Cu_{1.75}Se$ were fitted by pseudo-Voigt functions with the limiting cases of pure Lorentzian ($\eta = 1$) and Gaussian ($\eta = 0$) profiles ($pV(x) = \eta L(x) + (1\text{-}\eta)G(x)$, where $L(x)$ and $G(x)$ are the Lorentzian and

Table 5.2: The results of a Williamson-Hall plot.

Sample	Value of interception with ordinate axis (rad.)	Value of slope (rad.)	Volume weighted crystallite size (μ)	Weighted average strains (%)
$Cu_{1.75}Se$	0.0000(4)	0.00462(4)	~ 2	0.116
$Cu_{1.75}Se$ annealed	0.0000(2)	0.00107(2)	~ 2	0.027

Gaussian functions, respectively, and the parameter η ($0 \leq \eta \leq 1$) is the mixing ratio of *L(x)* and *G(x)* for a mixed profile). Figures 5.6 and 5.7 clearly show the essentially pure Lorentzian shape of observed diffraction lines. This fact allows quantitative Williamson-Hall analysis, based on FWHM(sinθ) only.

In order to illustrate the magnitude of peak broadening, FWHM *vs.* 2θ angle are plotted for three investigated samples: the reference standard material (LaB_6), annealed and non-annealed $Cu_{1.75}Se$ (figure 5.8). The values of FWHM lie on straight lines for $Cu_{1.75}Se$. This means that the broadening is mainly due to lattice strain. A conversion of the FWHM into the integral breadth (β) is needed, because unlike FWHM, the integral breadth β includes all data points of the line profile and can readily be interpreted in terms of microstructure parameters. The procedure for obtaining the integral breadth parameters from FWHM values is well described elsewhere (see for example [68, 72]). The Williamson-Hall plot for purely Lorentzian peaks is based on the following equation [72]:

$$(\beta_i - \beta_{ins}) \cos\theta_i = \frac{\lambda}{D_v} + 4\varepsilon \sin\theta_i \tag{5.1}$$

where β_i is the integral breadth (in radians) of the i-th Bragg-position at θ_i; D_v is the volume weighted crystallite size; ε is the weighted average strain; λ is the wave length and β_{ins} is the instrumental contribution to the peak breadth, approximated $\beta_{ins} = \beta_{LaB_6}$. The instrumental contribution was described by a 2-nd order polynomial dependence β_{LaB_6} *vs.* 2θ.

The resulting Williamson-Hall plot is shown in figure 5.8. This figure clearly presents an isotropic *hkl*-independent peak broadening effect, which cannot cause the shifts of Bragg-positions. The volume weighted crystallite size and average strain were calculated as values

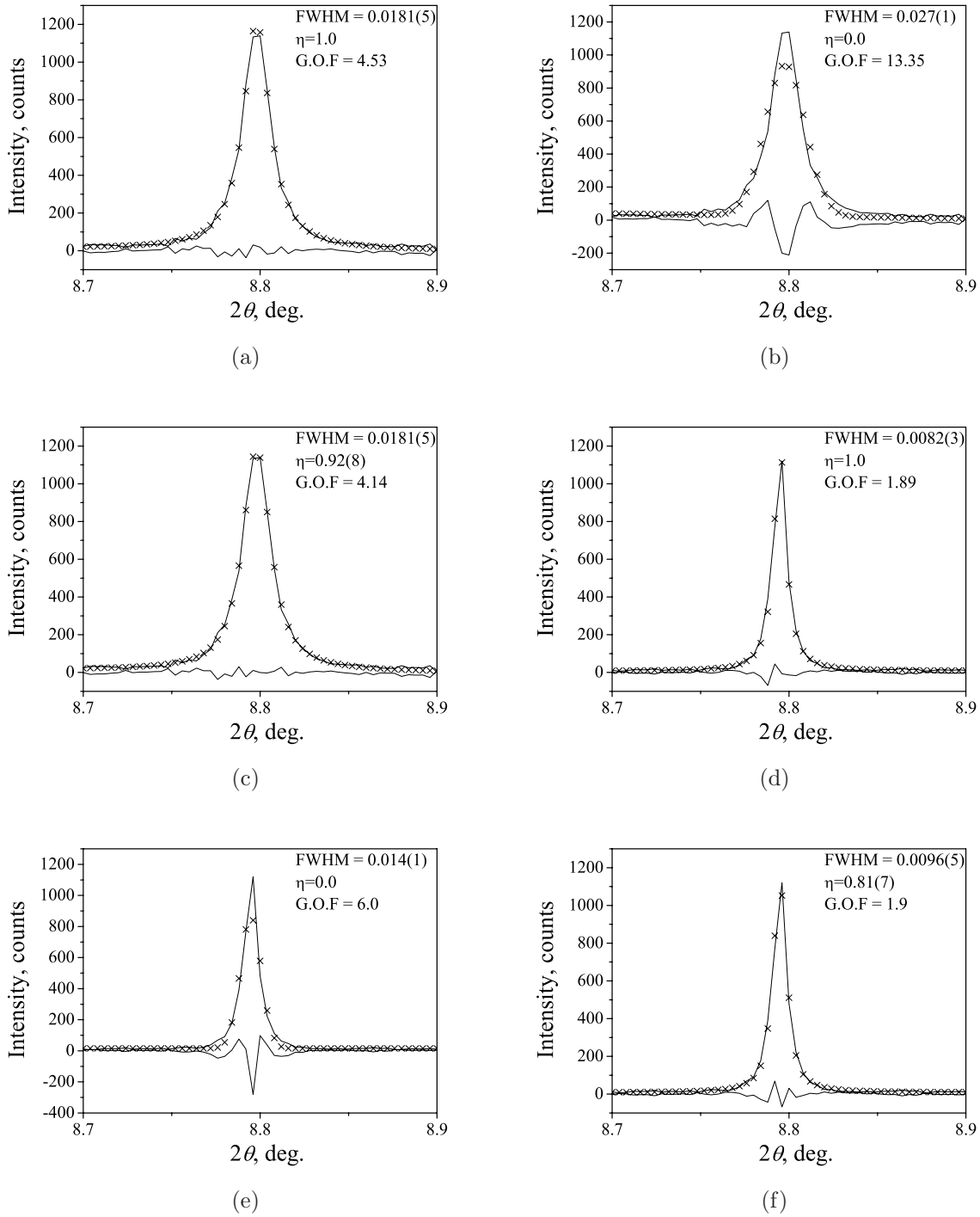

Figure 5.6: Profile fitting of the 100 lines from non-annealed (a-c) and annealed (d-f) β-$Cu_{1.75}Se$. Crosses are experimental data, lines calculated profiles and lower curves their differences.

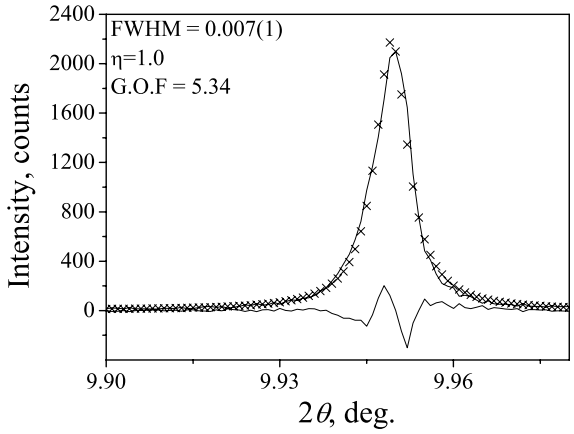

(a)

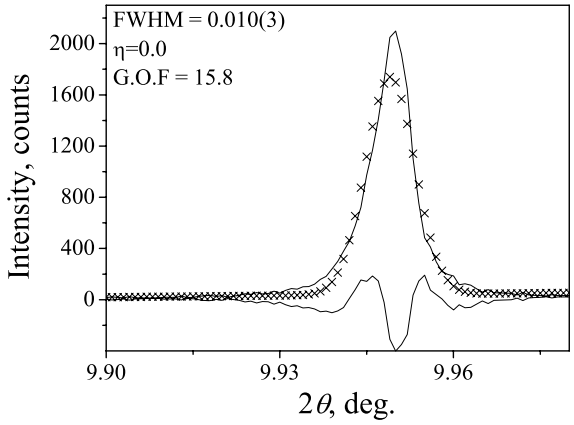

(b)

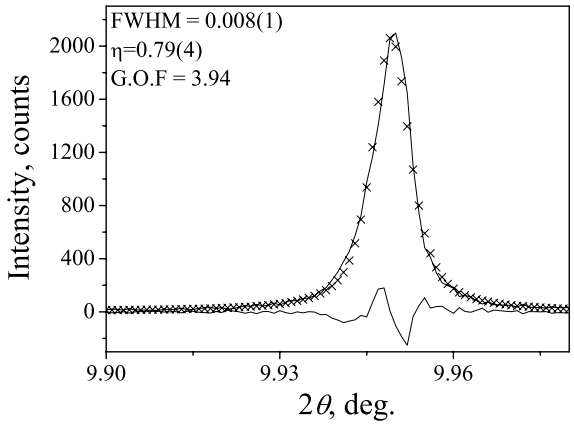

(c)

Figure 5.7: Profile fitting of the 110 diffraction lines from LaB_6. Crosses are experimental data, lines are calculated profiles and lower curves their differences.

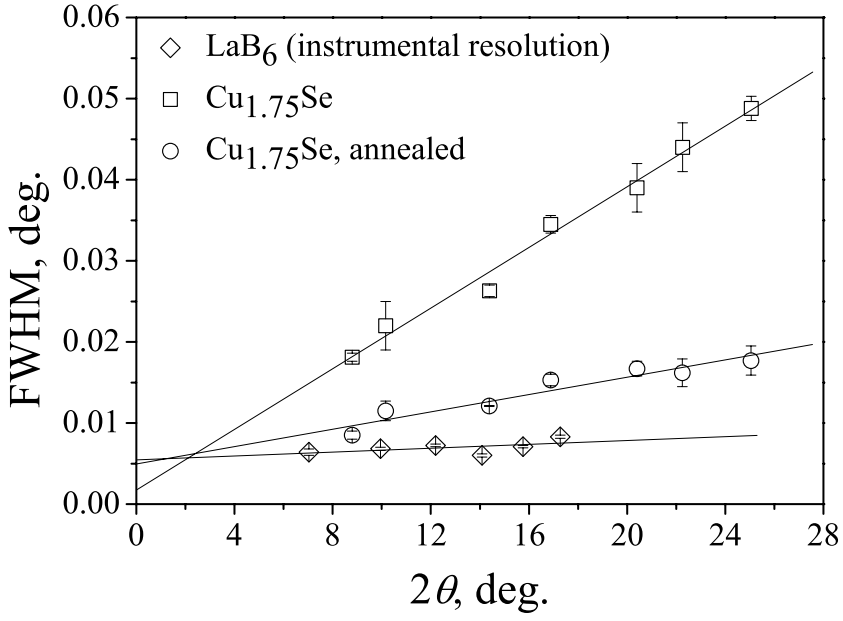

(a)

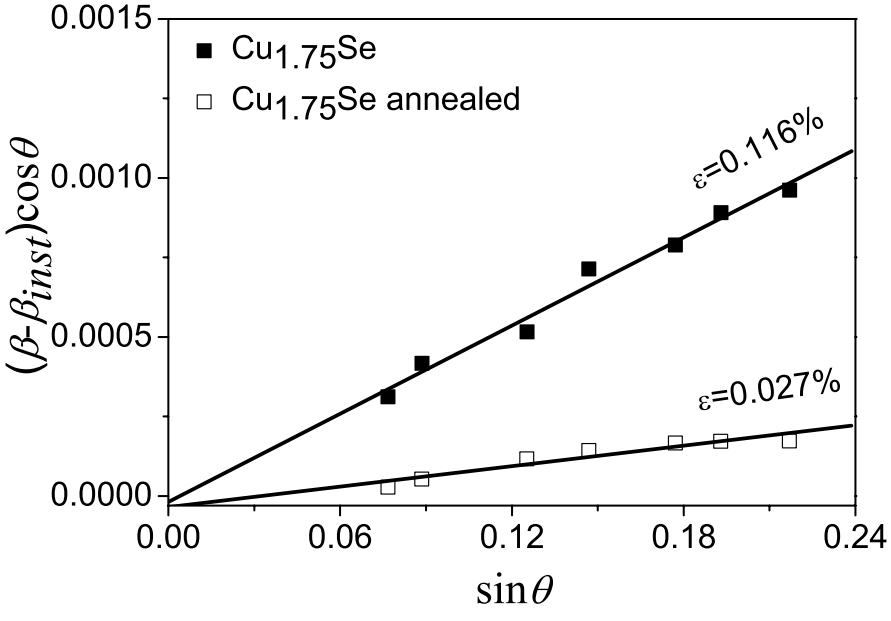

(b)

Figure 5.8: FWHM of annealed, non-annealed β-$Cu_{1.75}Se$ and LaB_6 reference material *vs.* 2θ (a) as well as a Williamson-Hall plot (b).

related with intercept and slope of the linear fit $(\beta_i - \beta_{ins})\cos\theta_i$ *vs.* $\sin\theta_i$, respectively (for clarity see equation 5.1 and [72]). Values of interceptions with ordinate axis and values of slopes as well as volume weighted crystallite size and average strains are summarized in table 5.2 for both samples. From this data it is evident that any contribution from a size-effect is negligible for the overall peak broadening, *i.e.*, volume weighted crystallite size of annealed and non-annealed β-$Cu_{1.75}Se$ is above the detection limit. Hence, the main reason of peak broadening in this case are strain effects. The weighted average strains, determined from the Williamson-Hall plots for annealed and non-annealed $Cu_{1.75}Se$, are 0.027% and 0.116%, respectively. The relatively small residual stress in the annealed sample is probably associated with the non-stoichiometry of the sample. This analysis by the Williamson-Hall approach confirms suggestion from Tonejc *et al.* [27] about the origin of peak broadening in $Cu_{2-\delta}Se$.

5.2 High-temperature synchrotron and neutron powder diffraction on eucairite, AgCuSe

5.2.1 Phase transitions and thermal expansion of AgCuSe

The high-temperature synchrotron powder diffraction measurements revealed two modifications of AgCuSe in the temperature range studied. Attempts to refine the structure of non-superionic β-AgCuSe based on the model from Frueh *et al.* (ICSD 44608, [42]) were unsuccessful. However, the diffraction patterns of β-AgCuSe could be indexed, according to the results from electron diffraction [47], based on a large orthorhombic supercell $a\times10a'\times2c$ with Z=40 (space group $Pmmn$), where a = 4.105 Å, a' = 4.070 Å, c = 6.310 Å are the lattice parameters at RT of the basic orthorhombic primitive subcell proposed by Frueh *et al.* [42]. In accordance with other authors [44,45,47,49], the high-temperature phase of silver copper selenide was indexed based on a cubic cell (space group $Fm\bar{3}m$, a=6.1002(8) Å at 523 K). The temperature dependence of lattice parameters and volume per formula unit of β- and α-AgCuSe are presented in figure 5.9. The discontinuous volume change of about 5% at the superionic $\beta \xrightarrow{480K} \alpha$ transition is a very strong indication for a 1st order phase

transition. Furthermore, the strong decrease of the Bragg intensity induced by this phase transition is evidence of a significant structural disorder in α-AgCuSe. The volume thermal expansion coefficients are $44{\cdot}10^{-6}\mathrm{K}^{-1}$ and $95{\cdot}10^{-6}\mathrm{K}^{-1}$ for the β- and α-phases, respectively.

5.2.2 Structural aspects of superionic α-AgCuSe

Synchrotron diffraction

The so called "split-site" analysis [2] was used to describe disorder in α-AgCuSe. During refinements great care was taken to ensure that data were not overinterpreted by models with an inappropriate large number of highly correlated structural parameters. The cation distribution was parameterized using different structural models with silver and copper cations randomly distributed over tetrahedral and octahedral interstitial sites within a rigid selenium fcc sublattice. Refinements were based on $Fm\overline{3}m$ symmetry and are summarized in table 5.3 and illustrated in figure 5.10. The results reflect a considerable degree of cation disorder which can be modelled by a random occupation of the tetrahedral 8(c) site at ($\frac{1}{4}$, $\frac{1}{4}$, $\frac{1}{4}$) and the octahedral 32(f) site at (x, x, x) with $\frac{1}{3}<x<\frac{1}{2}$ (table 5.3). This indicates cation disorder in $\langle 111\rangle$ directions. Attempts were also made to explain the data by an ideal antifluorite structure and a 'one-site' model with cations disordered in $\langle 111\rangle$ directions at 32(f) at (x, x, x) with $\frac{1}{4}<x<\frac{1}{3}$ sites. Furthermore, the following models with cations distributed between two sites were tested: 8(c) at ($\frac{1}{4}$, $\frac{1}{4}$, $\frac{1}{4}$) and 4(b) at ($\frac{1}{2}$, $\frac{1}{2}$, $\frac{1}{2}$) site (illustrates cation disorder in $\langle 111\rangle$ directions); 8(c) at ($\frac{1}{4}$, $\frac{1}{4}$, $\frac{1}{4}$) and 48(i) at (x, x, $\frac{1}{2}$) with $\frac{1}{3}<x<\frac{1}{2}$ sites (cation disorder in $\langle 110\rangle$ directions); between 8(c) at ($\frac{1}{4}$, $\frac{1}{4}$, $\frac{1}{4}$) and 48(g) at (x, $\frac{1}{4}$, $\frac{1}{4}$) with $\frac{1}{4}<x<\frac{1}{3}$ sites (cations are disordered in $\langle 100\rangle$ directions). All these models were either unstable in the refinement due to high correlations between fitted parameters or produced a poorer fit to the experimental data.

The model with cations disordered between 8(c) at ($\frac{1}{4}$, $\frac{1}{4}$, $\frac{1}{4}$) and 32(f) at (x, x, x) with $\frac{1}{3}<x<\frac{1}{2}$ yields a temperature dependence for the parameters of the average structure without any anomalies: isotropic temperature factors increase with increasing temperature (the temperature factors of the cations increase more rapidly); the cation positions of the octahedral site 32(f) at (x, x, x) with $\frac{1}{3}<x<\frac{1}{2}$ are slightly shifted from the centre of the octahedron; there are no pronounced changes in the temperature dependence of the cation

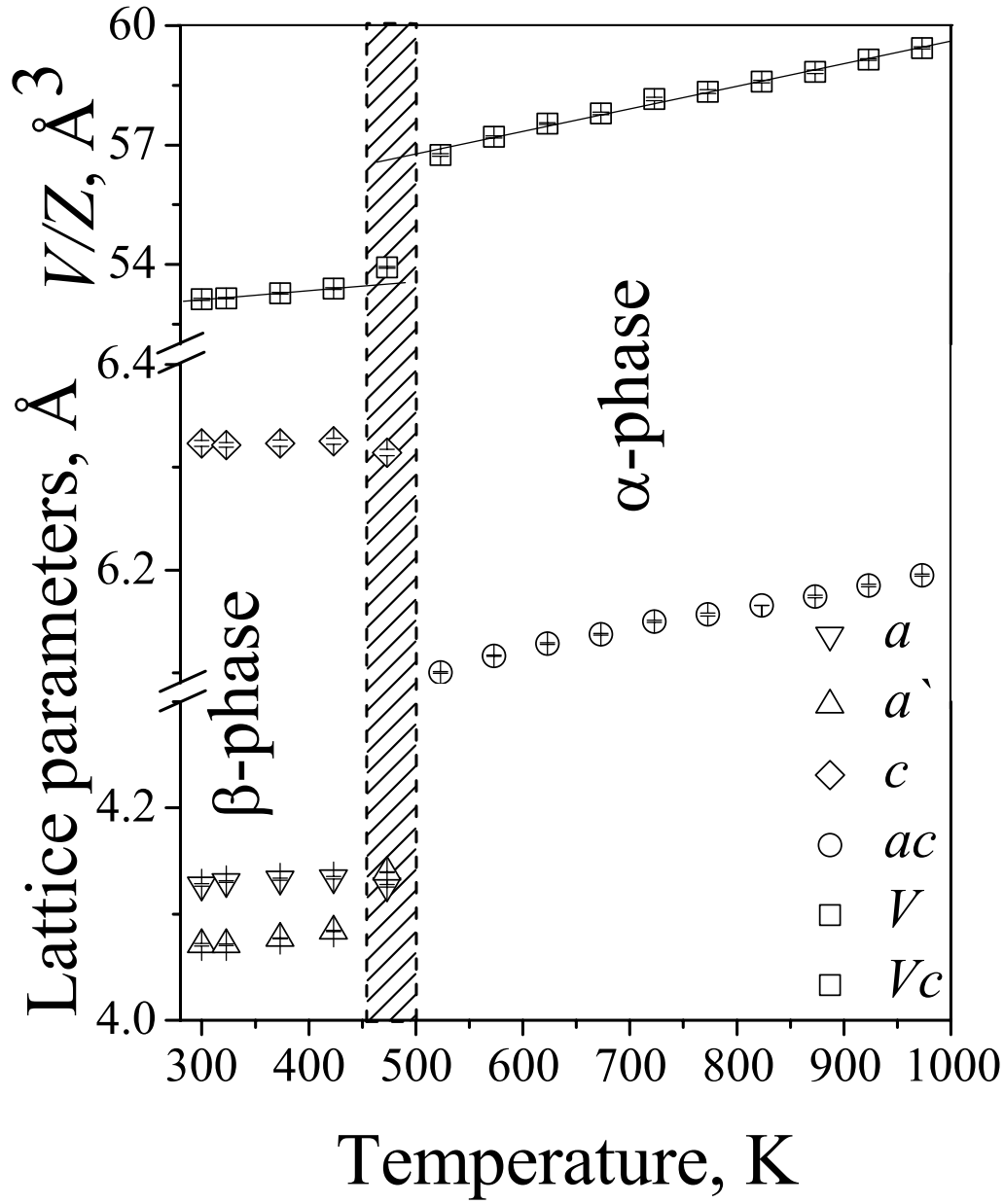

Figure 5.9: Temperature dependence of the lattice parameters of the basic orthorhombic subcell of β-AgCuSe (a – upside-down triangles, a‘– triangles, c – diamonds), cubic lattice parameter a_c of α-AgCuSe (circles) and the unit cell volume per formula unit (V/Z) of β- and α-AgCuSe (squares). The hatched region indicates the region in which the superionic phase transition takes place (as defined from the DCS curves).

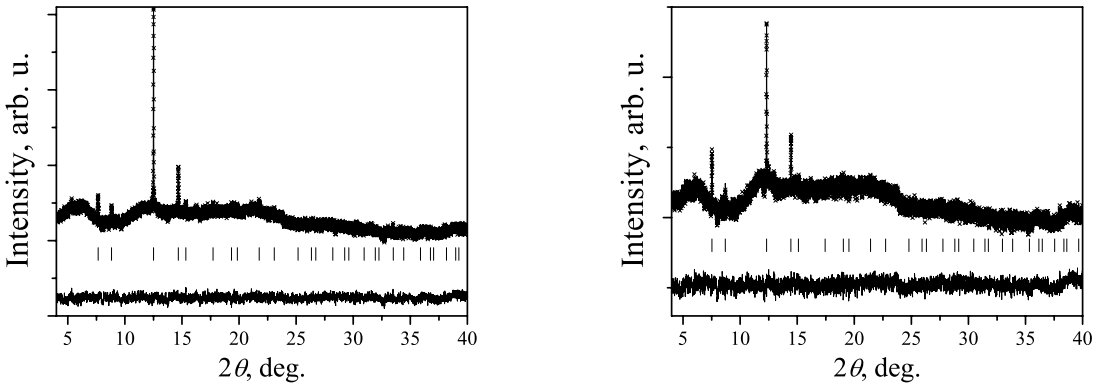

(a) α-AgCuSe at 523 K (b) α-AgCuSe at 973 K

Figure 5.10: Synchrotron powder diffraction patterns of α-AgCuSe ($\lambda = 0.47001$ Å). The Rietveld fits are based on the model with cations on tetrahedral 8(c) and octahedral 32(f) sites (see table 5.3). Crosses are experimental data, the lines are calculated profiles and the lower curves their difference. Tick marks show the calculated positions of α-AgCuSe reflections.

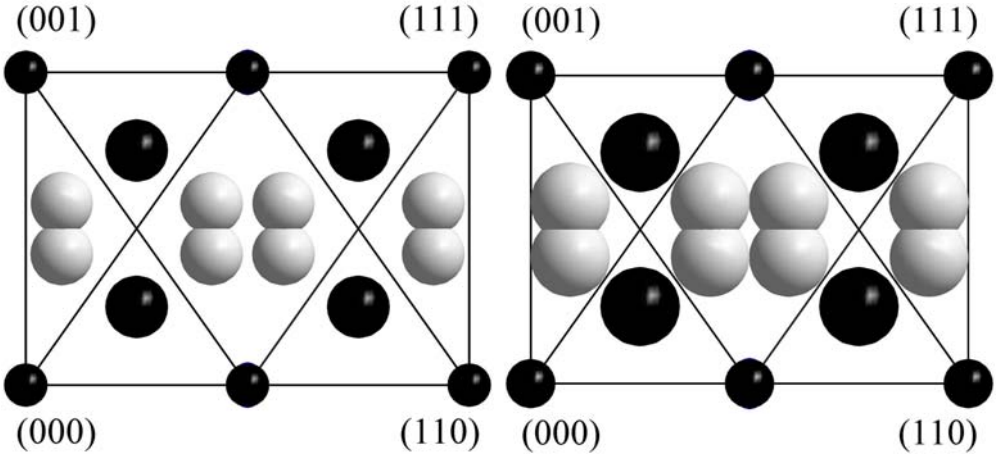

(a) α-AgCuSe at 523 K (b) α-AgCuSe at 973 K

Figure 5.11: Schematic representation of the average structure of α-AgCuSe according to model 4 from table 5.3. Plots show (110) section through the unit cell. Small dark spheres: anions on the 4(a) sites at (0, 0, 0), large dark spheres: cations on the ideal tetrahedral 8(c) sites at ($\frac{1}{4}$, $\frac{1}{4}$, $\frac{1}{4}$), bright spheres: cations on the octahedral 32(f) sites at (x, x, x) with $\frac{1}{3} < x < \frac{1}{2}$. The plots show 100% of occupancy for all crystallographically allowed cation positions. The diagonal lines indicate the positions of the boundaries between tetrahedral and octahedral interstices.

Table 5.3: Structural models of α-AgCuSe at lowest and highest experimental temperatures. Refined structural parameters: isotropic thermal displacements, cation positional parameters and cation site occupancies; cation isotropic thermal parameters and occupancies were constrained during refinements.

$Fm\bar{3}m$, Z=4, T=523 K, a=6.1002(8) Å						
Model, №	1	2	3	4	5	6
Se, site	4(a) at (0,0,0)					
u_{iso} (Å^2)	0.020(3)	0.023(3)	0.050(3)	0.076(5)	0.209(12)	0.067
Occupancy (%)	100	100	100	100	100	100
Ag/Cu, site	8(c)	32(f)	8(c)	8(c)	8(c)	8(c)
x	$\frac{1}{4}$	0.299(1)	$\frac{1}{4}$	$\frac{1}{4}$	$\frac{1}{4}$	$\frac{1}{4}$
y	$\frac{1}{4}$	0.299(1)	$\frac{1}{4}$	$\frac{1}{4}$	$\frac{1}{4}$	$\frac{1}{4}$
z	$\frac{1}{4}$	0.299(1)	$\frac{1}{4}$	$\frac{1}{4}$	$\frac{1}{4}$	$\frac{1}{4}$
u_{iso} (Å^2)	0.053(3)	0.001(3)	0.240(4)	0.158(6)	0.120(6)	0.128
Occupancy (%)	100	25	66.6(4)	53.1(8)	41.6(8)	96
Ag/Cu, site	–	–	4(b)	32(f)	48(i)	48(g)
x	–	–	$\frac{1}{2}$	0.419(2)	0.371(1)	0.300
y	–	–	$\frac{1}{2}$	0.419(2)	0.371(1)	$\frac{1}{4}$
z	–	–	$\frac{1}{2}$	0.419(2)	$\frac{1}{2}$	$\frac{1}{4}$
u_{iso} (Å^2)	–	–	0.240(4)	0.158(6)	0.120(6)	0.128
Occupancy (%)	–	–	66.8(8)	11.7(2)	9.7(1)	3
R_B	0.231	0.248	0.119	0.0357	0.0725	0.440
R_F	0.136	0.135	0.0918	0.0540	0.0764	0.573
χ^2	34.7	34.2	10.8	7.24	7.45	14.6
$Fm\bar{3}m$, Z=4, T=973 K, a=6.1950(11) Å						
Model, №	1	2	3	4	5	6
Se, site	4(a) at (0,0,0)					
u_{iso} (Å^2)	0.010(3)	0.022(5)	0.062(5)	0.104(6)	0.22(1)	0.008
Occupancy (%)	100	100	100	100	100	100
Ag/Cu, site	8(c)	32(f)	8(c)	8(c)	8(c)	8(c)
x	$\frac{1}{4}$	0.302(2)	$\frac{1}{4}$	$\frac{1}{4}$	$\frac{1}{4}$	$\frac{1}{4}$
y	$\frac{1}{4}$	0.302(2)	$\frac{1}{4}$	$\frac{1}{4}$	$\frac{1}{4}$	$\frac{1}{4}$
z	$\frac{1}{4}$	0.302(2)	$\frac{1}{4}$	$\frac{1}{4}$	$\frac{1}{4}$	$\frac{1}{4}$
u_{iso} (Å^2)	0.134(6)	0.037(7)	0.341(7)	0.268(6)	0.110(1)	0.126
Occupancy (%)	100	25	72.2(6)	52.0(4)	34(1)	96
Ag/Cu, site	–	–	4(b)	32(f)	48(i)	48(g)
x	–	–	$\frac{1}{2}$	0.410(2)	0.361(1)	0.300
y	–	–	$\frac{1}{2}$	0.410(2)	0.361(1)	$\frac{1}{4}$
z	–	–	$\frac{1}{2}$	0.410(2)	$\frac{1}{2}$	$\frac{1}{4}$
u_{iso} (Å^2)	–	–	0.341(7)	0.268(6)	0.110(1)	0.126
Occupancy (%)	–	–	55(1)	12.0(2)	8.4(2)	3
R_B	0.185	0.162	0.114	0.0695	0.0579	0.172
R_F	0.109	0.0923	0.0657	0.0391	0.0289	0.0955
χ^2	9.55	15.4	8.17	7.99	7.72	10.8

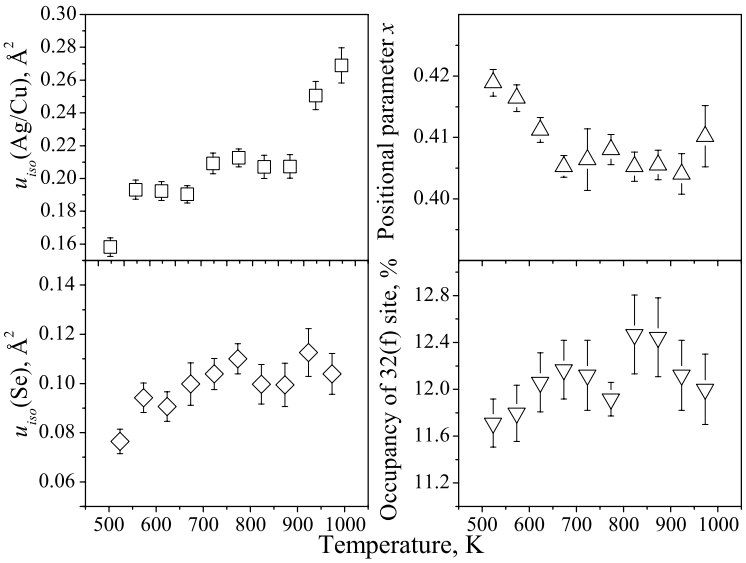

Figure 5.12: Temperature dependences of isotropic thermal parameters, normalized site occupation number of Ag^+/Cu^+ residing on the octahedral coordinated 32(f) sites and cation positional parameter of 32(f) at (x, x, x) sites within the cubic α-AgCuSe in the framework of model 4 from table 5.3.

occupancies (see figure 5.12). Within this model, disorder occurs in ⟨111⟩ directions towards the faces of the octahedron rather than to the octahedron edges; in spite of the significant octahedral occupation there is minimum cation density on the ideal octahedral site 4(b) at ($\frac{1}{2}$, $\frac{1}{2}$, $\frac{1}{2}$). In view of these crystal structure features, it is likely that cations jump in skewed ⟨100⟩ directions between nearest-neighbour tetrahedral sites *via* the peripheries of the octahedral cavities. The same mechanism of ionic conductivity was proposed on the basis of powder diffraction studies for the superionic antifluorite phases of Ag_2Te [86], $Cu_{2-\delta}Se$ (δ = 0, 0.15, 0.25) [57] and is obvious from analysis of diffraction results on CuI [87] and $Cu_{1.95}S$ [38]. Note that diffraction results on a number of copper- and silver- based halides and chalcogenides (for instance, [57,88,89]) imply that ionic conductivity can be sensitive to details of the cation redistribution between available interstitial sites *vs.* temperature or the stoichiometry of samples. Taking this into account, we can propose a correlation between the results of the electrochemical measurements from Miyatani *et al.* [12,13], which revealed only a relatively modest increase in ionic conductivity with temperature within α-AgCuSe, and diffraction results, which show no pronounced cation redistribution. The same correlation was reported for superionic fcc-$Ag_xPb_{1-x}I_{2-x}$ with x=$\frac{1}{3}$ and $\frac{2}{3}$ [88].

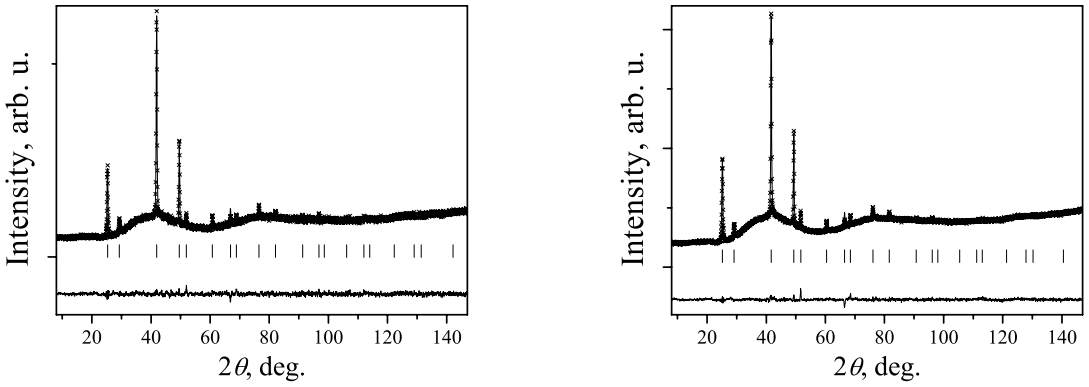

(a) α-AgCuSe at 610 K (b) α-AgCuSe at 773 K

Figure 5.13: Neutron powder diffraction patterns of superionic copper silver selenide collected at the SPODI diffractometer (λ=1.5487 Å). Comparison of observed and calculated profiles: the Rietveld fits are based on the model with cations distributed on tetrahedral and octahedral 32(f) sites (see table 5.4).

Neutron diffraction

Only 5 diffraction maxima were clearly visible in the synchrotron diffraction pattern of superionic α-AgCuSe. However, the temperature dependence of cation distribution in superionic α-AgCuSe as described by the structure model 4 from table 5.3 correlates well with the temperature behaviour of ionic conductivity and gives strong support for the validity of the model [48]. Despite this, neutron powder diffraction measurements were performed in order to elucidate more precisely the disorder in superionic α-AgCuSe. In this experiment 10 diffraction maxima were collected at two selected temperatures. The high diffuse background in α-AgCuSe is clearly observed in the diffraction patterns collected with SPODI. A very high background is also observed in the synchrotron diffraction patterns, especially in those measured with the image plate detector. This detector system has a high intrinsic background level and detects all kind of scattered radiation. It is therefore not possible to distinguish diffuse scattering from the sample from other contributions to the background quantitatively. The best structure models for α-AgCuSe as results of Rietveld refinements are summarized in table 5.4. A comparison of calculated and observed profiles is shown in figure 5.13. In summary, the results of neutron and synchrotron diffraction are consistent. Minor differences can be ascribed to the different scattering techniques and counting statistics in these experiments. The results from neutron diffraction confirm additionally the

Table 5.4: Structural parameters of α-AgCuSe as deduced from neutron diffraction data. Refined parameters: isotropic thermal displacements, cation positional parameters and cation site occupancies. The cation isotropic thermal parameters and occupancies were constrained to one common value.

$Fm\bar{3}m$, $Z = 4$, $T = 610$ K, $a = 6.1261(6)$ Å					
Model, №	1	2	3	4	5
Se, site	4(a) at (0,0,0)				
u_{iso} (Å^2)	0.082(2)	0.078(2)	0.105(1)	0.127(2)	0.124(2)
Occupancy (%)	100	100	100	100	100
Ag/Cu, site	8(c)	32(f)	8(c)	8(c)	8(c)
x	$\frac{1}{4}$		$\frac{1}{4}$	$\frac{1}{4}$	$\frac{1}{4}$
y	$\frac{1}{4}$		$\frac{1}{4}$	$\frac{1}{4}$	$\frac{1}{4}$
z	$\frac{1}{4}$		$\frac{1}{4}$	$\frac{1}{4}$	$\frac{1}{4}$
u_{iso} (Å^2)	0.159(3)	0.087(4)	0.297(3)	0.203(3)	0.211(4)
Occupancy (%)	100	25	56.1(6)	56.1(7)	59.2(6)
Ag/Cu, site	–	–	4(b)	32(f)	48(i)
x	–	–	$\frac{1}{2}$	0.404(1)	0.389(2)
y	–	–	$\frac{1}{2}$	0.404(1)	0.389(2)
z	–	–	$\frac{1}{2}$	0.404(1)	$\frac{1}{2}$
u_{iso} (Å^2)	–	–	0.297(3)	0.203(3)	0.211(4)
Occupancy (%)	–	–	87.1(6)	11.0(3)	6.8(2)
χ^2	2.60	3.46	1.87	1.49	1.58
$Fm\bar{3}m$, $Z = 4$, $T = 773$ K, a=6.1560(5) Å					
Model, №	1	2	3	4	5
Se, site	4(a) at (0,0,0)				
u_{iso} (Å^2)	0.071(5)	0.090(2)	0.083(2)	0.128(2)	0.124(2)
Occupancy (%)	100	100	100	100	100
Ag/Cu, site	8(c)	32(f)	8(c)	8(c)	8(c)
x	$\frac{1}{4}$	0.3058(4)	$\frac{1}{4}$	$\frac{1}{4}$	$\frac{1}{4}$
y	$\frac{1}{4}$	0.3058(4)	$\frac{1}{4}$	$\frac{1}{4}$	$\frac{1}{4}$
z	$\frac{1}{4}$	0.3058(4)	$\frac{1}{4}$	$\frac{1}{4}$	$\frac{1}{4}$
u_{iso} (Å^2)	0.196(5)	0.075(2)	0.284(4)	0.230(3)	0.239(5)
Occupancy (%)	100	25	56.1(6)	62.6(7)	60.6(7)
Ag/Cu, site	–	–	4(b)	32(f)	48(i)
x	–	–	$\frac{1}{2}$	0.400(1)	0.386(5)
y	–	–	$\frac{1}{2}$	0.400(1)	0.386(5)
z	–	–	$\frac{1}{2}$	0.400(1)	$\frac{1}{2}$
u_{iso} (Å^2)	–	–	0.284(4)	0.230(3)	0.239(5)
Occupancy (%)		–	87.8(7)	9.3(2)	6.6(2)
χ^2	6.79	4.32	5.36	3.40	3.91

model for the average structure from reference [48] (see also previous section).

5.3 High-temperature synchrotron and neutron powder diffraction on stromeyerite, AgCuS

5.3.1 Phase transitions and thermal expansion of AgCuS

The analysis of the structure evolution of AgCuS showed the following phase boundaries at elevated temperatures: orthorhombic ($Cmc2_1$) $\stackrel{361K}{\longrightarrow}$ hexagonal ($P6_3/mmc$) $\stackrel{399K}{\longrightarrow}$ hexagonal($P6_3/mmc$) plus cubic ($Fm\bar{3}m$) $\stackrel{439K}{\longrightarrow}$ cubic ($Fm\bar{3}m$). A large decrease in the Bragg intensities after the orthorhombic ($Cmc2_1$) $\stackrel{361K}{\longrightarrow}$ hexagonal ($P6_3/mmc$) phase transformation indicates a high degree of structural disorder in the hexagonal phase. The temperatures of the phase boundaries are in good agreement with the results presented in [55], but the structures of the different modifications of stromeyerite were insufficiently described in this reference. The analysis of the diffraction pattern from the sample after heat treatment in argon during the diffraction measurements, showed no changes with respect to the initial state.

In the latest work on the structure of stromeyerite by Baker *et al.* [50], for convenience, following the analogy with silver iodide, the low-temperature phase was labelled as γ-AgCuS, the RT phase β, and the cation-conducting high-temperature phase α. Nevertheless, it is not clear whether the hexagonal or the cubic high-temperature phase was denoted as α-AgCuS by Baker *et al.* To clarify this matter by following the notation accepted for other superionic conductors (see for instance [90]), the hexagonal structure of AgCuS should be denoted as α-AgCuS and the cubic phase at the temperature immediately above the α-phase should be denoted as δ-phase. Results of Rietveld refinements for selected temperatures for β-, α- and δ-AgCuS are illustrated in figure 5.14. Structure parameters for β- and α-AgCuS as derived in the present investigation are summarized in tables A.6, A.7 and agree well with the data from [50, 51] (see also tables 2.7 and 2.8). Models for the average structure of δ-AgCuS are summarized in the tables 5.5 and 5.6.

For convenience, the unit cell parameters a_{or}, b_{or}, c_{or} of the orthorhombic C-centered cell

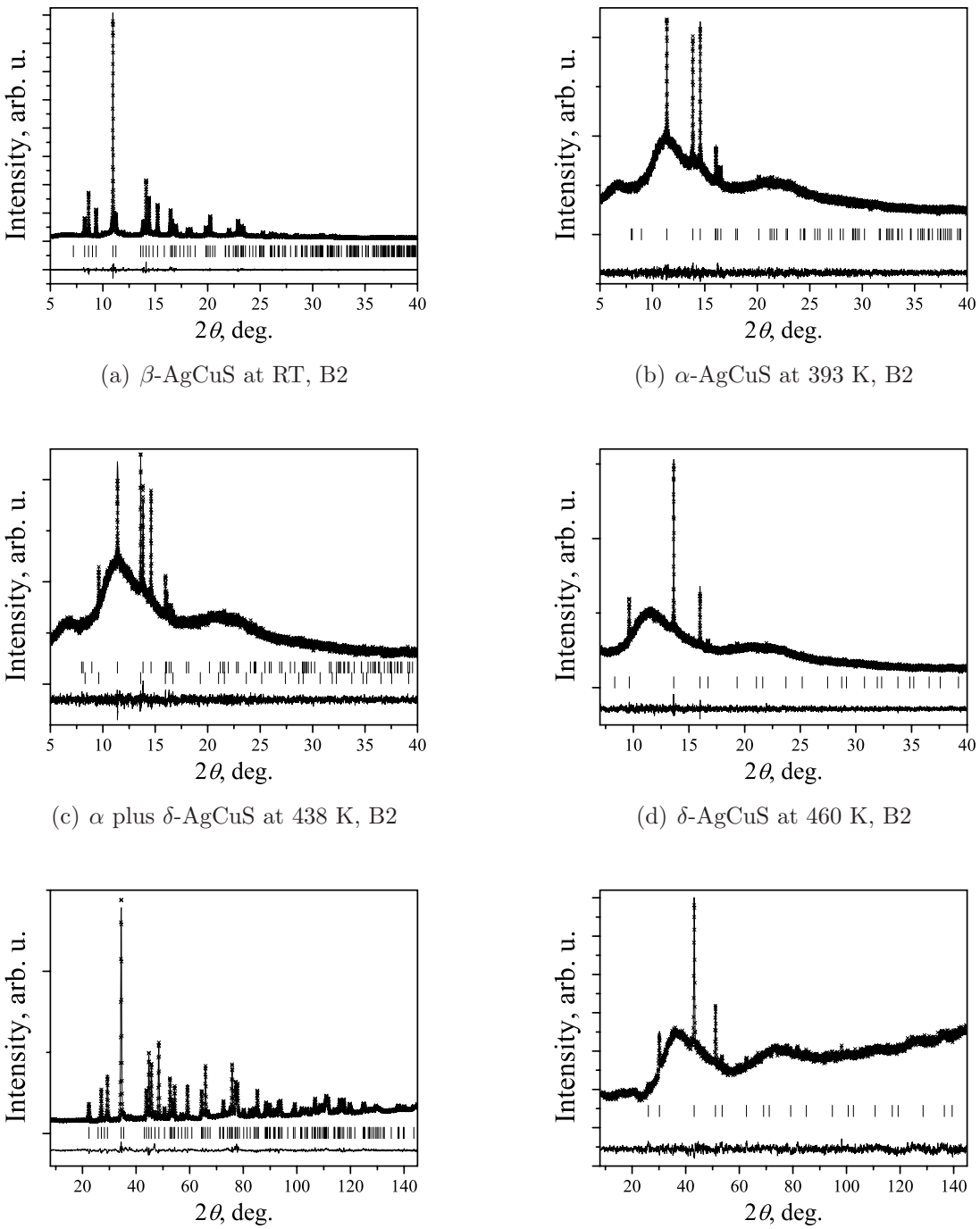

(a) β-AgCuS at RT, B2

(b) α-AgCuS at 393 K, B2

(c) α plus δ-AgCuS at 438 K, B2

(d) δ-AgCuS at 460 K, B2

(e) β-AgCuS at RT, SPODI

(f) δ-AgCuS at 460 K, SPODI

Figure 5.14: Results of Rietveld refinements for data collected with synchrotron (B2) and neutron (SPODI) radiation. Crosses are experimental data, the line through the crosses is the calculated profile and the lower curve their difference. Tick marks show the calculated positions of AgCuS reflections. The upper line of reflection marks in (c) belong to α-AgCuS, the lower line to δ-AgCuS.

of β-AgCuS were transformed into the primitive pseudo-hexagonal cell $\{ a_{phex}, b_{phex}, c_{phex}, 90^o, 90^o, \gamma_{phex} \}$ with $a_{phex}=b_{phex}=\sqrt{a_{or}^2 + b_{or}^2}/2$, $c_{phex}=c_{or}$ and $\gamma_{phex}=\arccos[(a_{or}^2 - b_{or}^2)/(a_{or}^2 + b_{or}^2)]$. The unit cell parameter of cubic fcc δ-AgCuS was transformed into the primitive rhombohedral one *via* $a_{rh}=\sqrt{2}a_c/2$, where a_{rh} and a_c are the cell dimensions of the rhombohedral and cubic cells, respectively.

The unit dimensions of the primitive cells, cell axial ratio and unit cell volume per formula unit of stromeyerite as a function of temperature are illustrated in figure 5.15. Analysis of the thermal behaviour of the lattice parameters revealed a strong anisotropy of thermal expansion in β- and α-AgCuS. A negative thermal expansion was observed in c-direction for both phases between 316 and 440 K. The positive thermal expansion in β-AgCuS along the c-direction at RT changed into a negative value above 316 K (see inset in figure 5.15). No anomalies in the thermal expansion in a-direction were revealed in the range RT - 399 K. With entering the coexistence range of α and δ phase above 399 K the thermal expansion of α-AgCuS in a-direction suddenly reverses sign and remains negative up to 439 K. Similarly, the thermal expansion coefficient of δ-AgCuS is negative in the α and δ region, but positive for the pure δ phase. Additionally, the axial c/a ratio in pseudo-hexagonal β-AgCuS and hexagonal α-AgCuS is an appropriate measure for the deviation from an ideal hcp structure and decreases with increasing temperature, approaching the 'ideal' value of 1.633 for a close-packed structure. An increase in temperature results in a decrease of the hexagonal distortion in both the β- and α-phases. The drop in the c/a-value is drastically reduced in the mixed two phase (α and δ) region. The discontinuous volume changes of about 2.3% and 0.6% at the $\beta \longrightarrow \alpha$ and $\alpha \longrightarrow \delta$ transformations, respectively, as well as the observed two phase (α and δ) coexistence range are very strong indications for 1st order phase transitions. The temperature dependence of the volume thermal expansion for all phases was fitted by linear functions and the volume thermal expansion coefficients are $26 \cdot 10^{-6} K^{-1}$, $130 \cdot 10^{-6} K^{-1}$ and $85 \cdot 10^{-6} K^{-1}$ for the β-, α- and δ- phases, respectively. A negative expansion of the cell volumes of hexagonal and cubic stromeyerite was revealed in the two phase (α and δ) region. An extrapolation of the cell volumes of the pure α- and δ-phases into the α plus δ region gives larger volume for the α-phase than for the δ-phase, but throughout this region the experimentally observed cell volume of α-AgCuS is even lower than the extrapolated one for